Check for updates

Rise and fall of Landau's quasiparticles while approaching the Mott transition

Andrej Pustogow [1,2,6✉], Yohei Saito[1,3], Anja Löhle[1], Miriam Sanz Alonso[1], Atsushi Kawamoto [3], Vladimir Dobrosavljević [4], Martin Dressel [1✉] & Simone Fratini [5✉]

Landau suggested that the low-temperature properties of metals can be understood in terms of long-lived quasiparticles with all complex interactions included in Fermi-liquid parameters, such as the effective mass $m^\star$. Despite its wide applicability, electronic transport in bad or strange metals and unconventional superconductors is controversially discussed towards a possible collapse of the quasiparticle concept. Here we explore the electrodynamic response of correlated metals at half filling for varying correlation strength upon approaching a Mott insulator. We reveal persistent Fermi-liquid behavior with pronounced quadratic dependences of the optical scattering rate on temperature and frequency, along with a puzzling elastic contribution to relaxation. The strong increase of the resistivity beyond the Ioffe–Regel–Mott limit is accompanied by a 'displaced Drude peak' in the optical conductivity. Our results, supported by a theoretical model for the optical response, demonstrate the emergence of a bad metal from resilient quasiparticles that are subject to dynamical localization and dissolve near the Mott transition.

[1] 1. Physikalisches Institut, Universität Stuttgart, 70569, Stuttgart, Germany. [2] Department of Physics and Astronomy, UCLA, Los Angeles, CA, USA. [3] Department of Physics, Graduate School of Science, Hokkaido University, Sapporo, Japan. [4] Department of Physics and National High Magnetic Field Laboratory, Florida State University, Tallahassee, FL, USA. [5] Institut Néel - CNRS and Université Grenoble Alpes, Grenoble Cedex 9, France. [6] Present address: Institute of Solid State Physics, Vienna University of Technology, Vienna, Austria. ✉email: pustogow@ifp.tuwien.ac.at; dressel@pi1.physik.uni-stuttgart.de; simone.fratini@neel.cnrs.fr

Conduction electrons in solids behave differently compared to free charges in vacuum. Since it is not possible to exhaustively model the interactions with all constituents of the crystal (nuclei and other electrons), Landau postulated quasiparticles (QP) with charge e and spin $\frac{1}{2}$, which can be treated as nearly free electrons but carry a renormalized mass $m^\star$ that incorporates all interaction effects[1]. In his Fermi-liquid picture, the conductivity of metals scales with the QP lifetime τ, which increases asymptotically at low energy as the scattering phase space shrinks to zero[1]. Electron–electron interaction involves a quadratic energy dependence of the scattering rate $\gamma = \tau^{-1}$ on both temperature T and frequency ω[2–5], expressed as:

$$\gamma(T, \omega) = \gamma_0 + B\left[(p\pi k_B/\hbar)^2 T^2 + \omega^2\right]. \qquad (1)$$

Here γ_0 stems from residual scattering processes at zero energy (e.g., impurities), and p is a numerical constant; the coefficient B controls the overall rate of variation with energy and increases with the effective mass $m^\star$. In most metals with large electronic bandwidth W the behavior described by Eq. (1) is not seen because of the small $m^\star$, so that the intrinsic contribution to scattering is negligible compared to other sources of dissipation (Fig. 1). Electronic correlations can strongly enhance the effective mass, $m^\star/m_b \gg 1$ (in a local Fermi liquid the QP weight scales as $Z \propto (m^*/m_b)^{-1}$, where m_b is the band mass), making the energy-dependent terms of Eq. (1) the dominant contributions in the dc resistivity $\rho(T)$ and optical conductivity $\sigma_1(\omega)$.

While the quasiparticle concept has proven extremely powerful in describing good conductors, QPs become poorly defined in case of excessive scattering. In metals, the scattering rate is expected to saturate when the mean free path approaches the lattice spacing, known as Ioffe–Regel–Mott (IRM) limit[6,7]. However, this bound is often exceeded ($\rho \gg \rho_{IRM}$) in correlated, 'Mott' systems[8]. In view of the apparent breakdown of Boltzmann transport theory, it is controversially discussed whether charge transport in such *bad metals*[6,7] is in any way related to QPs[9–11] or whether entirely different excitations come into play[12]. By investigating the low-energy electrodynamics of a strongly correlated metal through comprehensive optical measurements, here
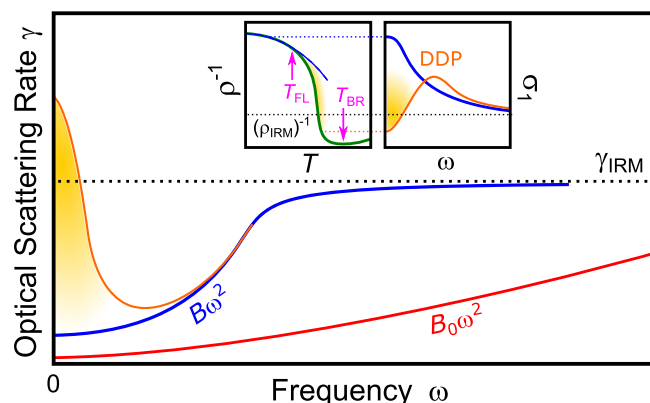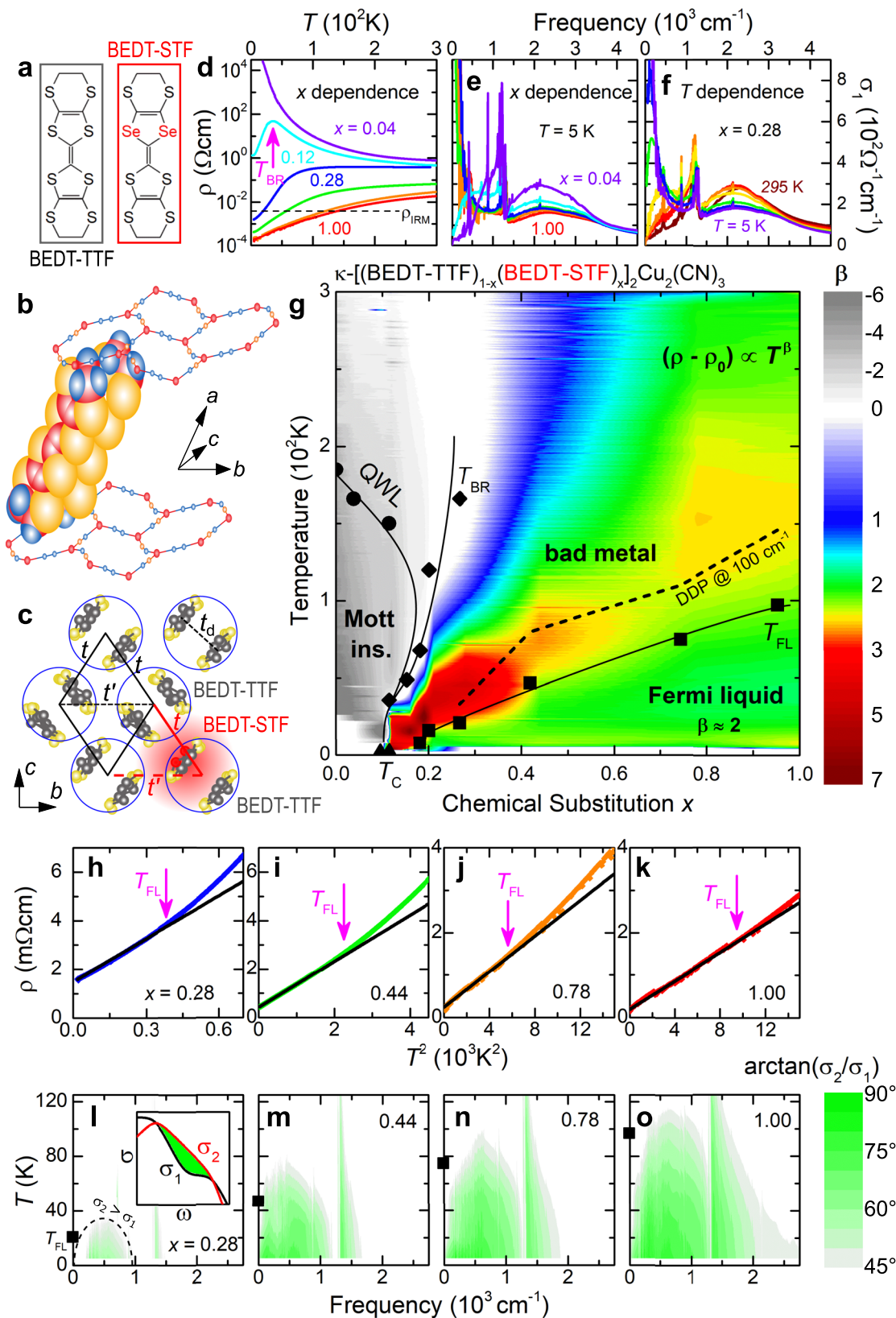
we uncover the prominent role of QPs persisting into this anomalous transport regime, providing evidence for the former scenario. Our results also demonstrate the emergence of a 'displaced Drude peak' (DDP, see inset of Fig. 1) indicating incipient localization of QPs in a regime where their lifetime is already heavily reduced by strong electronic interactions.

Results

We have chosen the molecular charge-transfer salts κ-[(BEDT-STF)$_x$(BEDT-TTF)$_{1-x}$]$_2$Cu$_2$(CN)$_3$ (abbreviated κ-STF$_x$), which constitute an ideal realization of the single-band Hubbard model on a half-filled triangular lattice. In the parent compound of the series ($x = 0$), strong on-site Coulomb interaction $U = 2000$ cm^{-1} (broad maximum of $\sigma_1(\omega)$ in Fig. 2e, f) gives rise to a genuine Mott-insulating state[13,14] with no magnetic order[15] down to $T = 0$. Partial substitution of the organic donors by Se-containing BEDT-STF molecules with more extended orbitals[16] increases the transfer integrals $t \propto W$ (Fig. 2a–c). As a result, the correlation strength U/W is progressively reduced with x, allowing us to tune the system through the "bandwidth-controlled" Mott metal-insulator transition (MIT), covering a wide range in $k_B T/W$ and $\hbar\omega/W$ within the parameter ranges accessible in our transport and optical experiments (see Supplementary Notes 2 and 3).

$\rho(T)$ of κ-STF$_x$ (Fig. 2d) reveals a textbook Mott MIT resembling the pressure evolution of κ-(BEDT-TTF)$_2$Cu$_2$(CN)$_3$[17–19], which turns metallic around 1.3 kbar. As x rises further, Fermi-liquid behavior $\rho(T) = \rho_0 + AT^2$ stabilizes below a characteristic T_{FL} that increases progressively with x, while $A \propto (m^\star)^2$ is reduced[20] as correlations diminish (Fig. 2h–k). As common for half-filled Mott systems[10,21], $\rho(T)$ rises faster than T^2 above T_{FL}, seen by the effective temperature exponent $\beta \gg 2$ in Fig. 2d, and exceeds $\rho_{IRM} = hd/e^2 = 4$ mΩ cm ($h = 2\pi\hbar$ is Planck's constant, e the elementary charge, and $d = 16$ Å the inter-layer spacing). We note that the bad metal formed here does not exhibit a linear-in-T resistivity that occurs in many other materials[12]. Instead, metallic behavior is completely lost when temperature exceeds the kinetic energy of QPs at the Brinkman–Rice scale $k_B T_{BR} \simeq Z E_F$[9,22], and $\rho(T)$ resembles a thermally activated semiconductor above the resistivity maximum[23,24]. Also in the optical conductivity we observe the transition from an insulator ($d\sigma_1/d\omega > 0$ at low frequencies) to a metal ($d\sigma_1/d\omega \leq 0$), forming a QP peak at $\omega = 0$ upon increasing x and lowering T (Fig. 2e, f). The phase diagram in Fig. 2g summarizes the characteristic crossovers in κ-STF$_x$ (black symbols), also including the quantum Widom line (QWL)[13,21,25] that separates the Mott insulator with a well-defined spectral gap from the incoherent semiconductor at elevated temperatures.

The low-energy response of Fermi liquids and the corresponding quadratic scaling laws are well explored theoretically[2–5]. A scattering rate $\gamma \propto \omega^2$ implies an inductive response characterized by $\sigma_2 > \sigma_1$, where σ_1 and σ_2 are the real and imaginary part of the optical conductivity, respectively. This occurs in the so-called 'thermal' regime[4], $\omega > \gamma$, delimited by semi-elliptical regions in $T - \omega$ domain, as recently reported in Fe-based superconductors[26]. Our optical data on κ-STF$_x$ indeed reveal inductive behavior, signaled by characteristic semi-ellipses with a phase angle $\arctan(\sigma_2/\sigma_1) > 45°$ (Fig. 2l–o), and occurring at temperatures where $\rho \propto T^2$ is seen in dc transport (Fig. 2h–k), i.e., at $T < T_{FL}$ (black squares). Concerning the ω^2/T^2 scaling in Eq. (1), Fermi-liquid theory predicts a 'Gurzhi parameter' $p = 2$ for the optical scattering rate $\gamma(T, \omega)$[2], a quantity that can be extracted from the optical conductivity via extended Drude analysis. Experimentally, values both in the range $1 \leq p \leq 2$[26–29] and $p \geq 2$[30] have been found for $\gamma(T, \omega)$ in few selected materials.

Fig. 1 Scattering rate of correlated metals. In a Fermi liquid $\gamma(T, \omega)$ scales with T^2 and ω^2 due to the increase in scattering phase space (Eq. (1)). In common metals, electron–electron scattering is weak (red) and other dissipation processes dominate. The ω^2 dependence prevails (blue) as electronic correlations yield $B \gg B_0$. While in good metals $\gamma(T, \omega)$ saturates at the Ioffe–Regel–Mott (IRM) limit[6,7], dynamical localization[35] can exceed this bound at low frequencies (orange). Insets: At $T < T_{FL}$ the quasiparticle peak in the optical conductivity σ_1 occurs at $\omega = 0$. At $T_{FL} < T < T_{BR}$, the resistivity (green, ρ^{-1} shown to compare with σ_1) deviates from $\rho \propto T^2$ (blue) and increases beyond ρ_{IRM}, which yields a drop of σ_1 at low frequencies, forming a 'displaced Drude peak' (DDP) in a bad-metallic state.

While purely inelastic scattering among QPs yields $p = 2$, deviations towards $p = 1$ have been assigned to elastic scattering off quasi-static impurities (dopants, f-electrons), for instance[5]. It remains an open question how the T and ω dependences, and the value of p, develop as correlations advance towards the Mott MIT.

In κ-STF$_x$, the broadband response follows $\gamma \propto \omega^2$ at low T (Fig. 3), as expected from Eq. (1), in all the compounds of the series ($x = 0.28$, 0.44, 0.78, and 1.00) that also show Fermi-liquid behavior in $\rho(T)$. The pronounced dip visible in the spectra around 1200 cm^{-1} stems from a vibration mode with Fano-like shape in $\sigma_1(\omega)$ and does not affect the relevant low-frequency

Fig. 2 Mott transition to bad metal and Fermi liquid. a–c Introducing selenium-containing BEDT-STF molecules (red) in the layered triangular-lattice compound κ-(BEDT-TTF)$_2$Cu$_2$(CN)$_3$ locally increases the transfer integrals. **d** This enhancement of electronic bandwidth by chemical substitution x yields a textbook-like Mott MIT in the resistivity of κ-STF$_x$. **e, f** The optical conductivity reveals the formation of a correlated metallic state when increasing x and reducing T. **g** Consistent with theory (see Fig. 3 of ref. [21]), the resistivity exponent $\beta = d(\ln\{\rho - \rho_0\})/d(\ln\{T\})$ shows large negative values in the Mott-insulating state (gray) below the quantum Widom line (QWL). On the metallic side, Fermi-liquid like $\rho = \rho_0 + AT^2$ at low temperatures (green) crosses over to a bad metal above T_{FL}, featuring a rapid increase beyond ρ_{IRM}. $\beta \gg 2$ (orange-red) coincides with the displacement of the Drude peak from $\omega = 0$ (DDP, dashed line). Metallic behavior is lost at T_{BR}, where $\rho(T)$ has a maximum. **h–k** The AT^2 increase becomes steeper towards the MIT. **l–o** The phase angle determined from our optical experiments yields inductive semi-ellipses (arctan$\{\sigma_2/\sigma_1\} > 45°$ corresponds to $\sigma_2 > \sigma_1$) in $T - \omega$ domain as expected for a paradigmatic Fermi liquid[4,26]. The sharp feature occuring for all compounds at 1200 cm^{-1} is a vibration mode (see Supplementary Fig. 5).
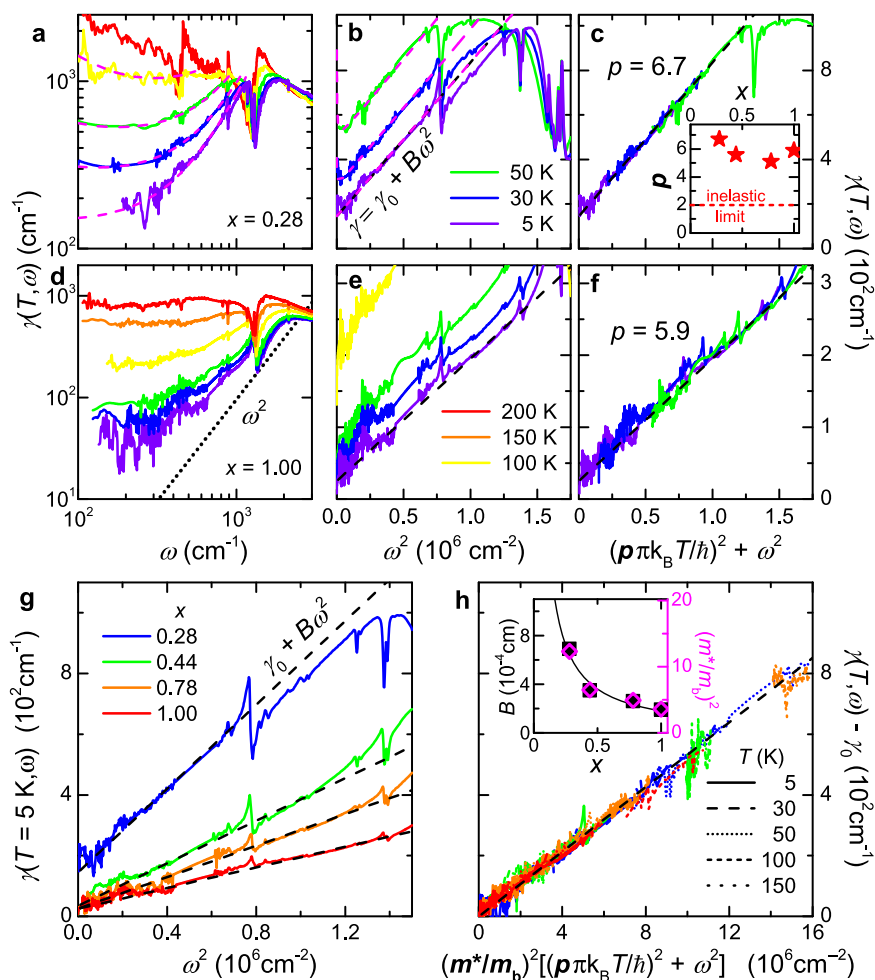

Fig. 3 Fermi-liquid scaling of optical scattering rate obtained from extended Drude analysis. a, d $\gamma(T, \omega)$ acquires a pronounced frequency dependence at low T, here shown for $x = 0.28$ and 1.00. **b, e** ω^2 behavior persists well above T_{FL}; note the quadratic frequency scales. Dashed pink lines in **a, b** are fits to Eq. (2). **c, f** Curves recorded at different T collapse on a generalized quadratic energy scale (see Eq. (1)) for a specific Gurzhi parameter $p > 2$, as shown in the inset. **g** Comparing $\gamma(\omega)$ at 5 K for $x \geq 0.28$ reveals that the slope of $B\omega^2$ increases towards the Mott MIT, similar to AT^2 in dc transport (Fig. 2h–k). **h** Rescaling the energy dependence by $(m^\star/m_b)^2$ (see Supplementary Fig. 10) collapses all data on a universal scaling curve, which follows from $B \propto (m^\star/m_b)^2$. The 5, 30, and 50 K data are shown for all four substitutions (color code like in **g**); the scaling holds even for $T \geq 100$ K for $x \geq 0.44$. In panels **b, c, e, f, h** only the range below the vibrational features at 880 or 1200 cm^{-1} is considered.

behavior (see Fig. 2e, f and Supplementary Fig. 5). Analogue to the increase of the slope A in Fig. 2h–k, the ω^2 variation of the scattering rate also becomes steeper as correlations gain strength (Fig. 3g), i.e., the coefficient B increases as x is reduced. In both cases, the quadratic energy dependence (and any dγ/d$\omega > 0$) appears only below $\gamma_{IRM} = 1000$ cm^{-1}.

The stringent prediction Eq. (1) can be directly verified by adding the T^2- and ω^2-dependences of $\gamma(T, \omega)$ to a common energy scale. In Fig. 3c, f, the curves at different T do fall on top of

each other upon scaling via a Gurzhi parameter $p = 6 \pm 1$ for all κ-STF$_x$ (see inset of panel c and Supplementary Fig. 11e–h). Even more striking, multiplying the energy scale by $(m^\star/m_b)^2$ collapses the data of all four substitutions on one universal line (Fig. 3h). This manifestation of the Kadowaki–Woods relation[20], $B \propto (m^\star)^2$ (see inset), rules out any relevance of spinons near the Mott MIT[19,31], in accord with dynamical mean-field theory (DMFT) results[32]. All in all, the observed scaling provides compelling evidence for the applicability of Landau's Fermi-liquid
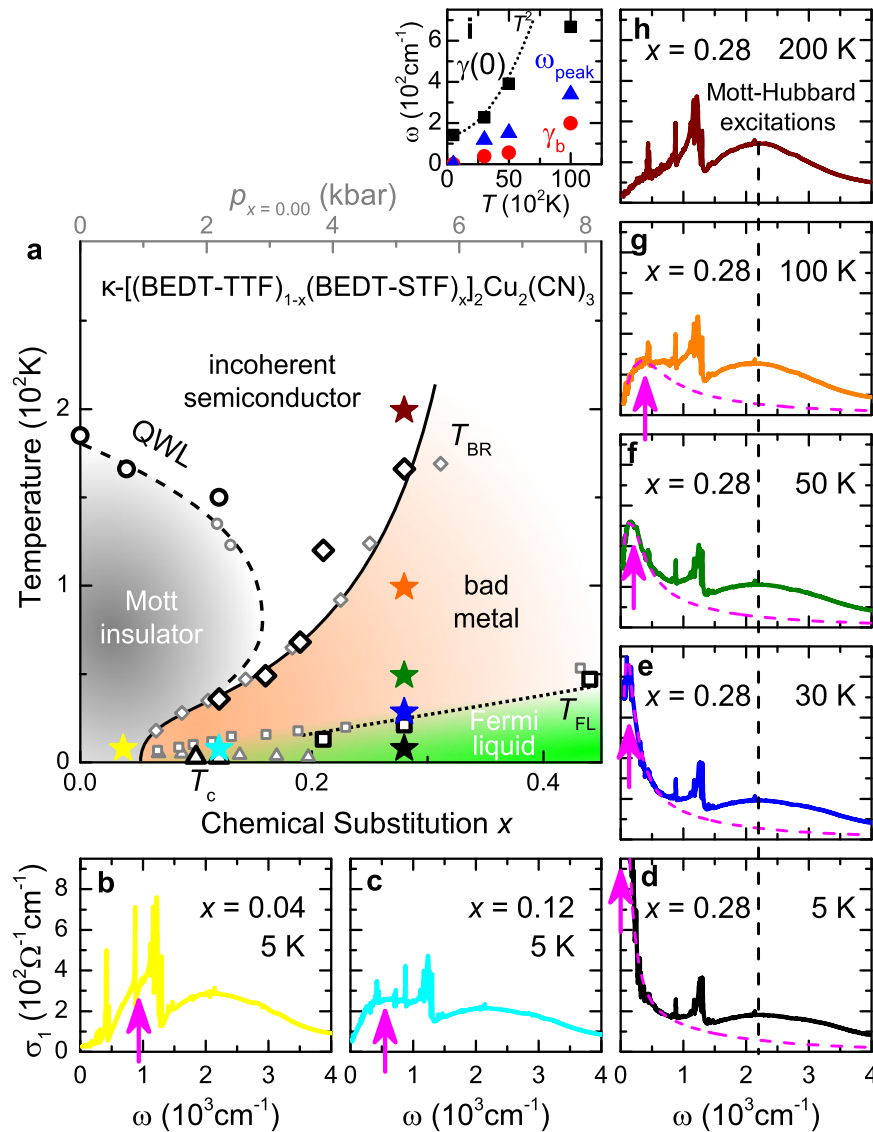
Fig. 4 Displaced Drude peak linked to bad metal. a Chemical substitution x (black symbols) and physical pressure p (gray, see Supplementary Fig. 2) have the same effect on κ-(BEDT-TTF)$_2$Cu$_2$(CN)$_3$[24]. **b–h** Evolution of $\sigma_1(T, \omega, x)$ through the phase diagram; stars with respective color indicate the position in **a**. Entering the bad-metallic phase for $T > T_{FL}$ shifts the Drude peak away from $\omega = 0$. The maximum broadens and hardens with T, until it dissolves at T_{BR}. Approaching the insulator ($x = 0.28 \rightarrow 0.04$) at low T, the QP feature transforms into finite-frequency metallic fluctuations within the Mott gap[13]. **i** Fit parameters (Eq. (2)) for dashed pink lines in **d–g** and Fig. 3a, b. Dotted line indicates $\gamma(0) = \gamma_0 + B(p\pi k_B T/\hbar)^2$, with B and p from Fig. 3.

concept, in agreement with previous studies on unconventional superconductors[26,28,29]. The Gurzhi parameter significantly exceeds the inelastic limit ($p = 2$)[5], indicating quasi-elastic backscattering processes (see Eqs. (2) and (3) below).

Having analyzed the QP properties and their dependence on electronic correlations, we now want to evaluate how they behave when scattering increases as we cross over from the Fermi liquid into a bad metal. Figure 4 displays $\sigma_1(\omega)$ at distinct positions in the T–x phase diagram (stars in panel a); note the similarity between κ-STF$_x$ (black symbols) and κ-(BEDT-TTF)$_2$Cu$_2$(CN)$_3$ subject to pressure tuning (gray). For all $x \geq 0.28$ and $T < T_{FL}$, the optical spectra feature a Drude-like peak centered at $\omega = 0$, representing the QP response, together with a broad absorption centered at $U = 2000\,\mathrm{cm}^{-1}$ originating from electronic transitions between the Hubbard bands[13], as shown in Fig. 4d (see also Fig. 2e, f and Supplementary Fig. 6). While the high-energy features show only weak dependence on x and T, a marked shift of spectral weight takes place within the low-frequency region

(see Supplementary Note 3). The fingerprints of mobile carriers evolve upon moving away from the Fermi-liquid regime by either changing x (Fig. 4b–d) or increasing T (d-h), until they completely disappear both in the Mott insulator (panel b) and in the incoherent semiconductor (panel h, $T > T_{BR} = 166$ K at $x = 0.28$).

Closer scrutiny reveals that this gradual evolution of the low-frequency absorption is accompanied by the appearance of a dip at $\omega = 0$, which occurs at $T \geq T_{FL}$; this is also where the resistivity becomes anomalous, deviating from $\rho \propto T^2$. The QP response then evolves into a finite-frequency peak, that steadily shifts to higher ω and broadens with increasing T/reducing x (arrows in Fig. 4e–g and triangles in panel i). Such a displaced Drude peak eventually dissolves into the Hubbard band at $T \sim T_{BR}$. From contour plots of $\sigma_1(T, \omega)$ in Supplementary Fig. 7 we can estimate the T–ω trajectory of the DDP above T_{FL} for the different substitutions: a peak frequency around $100\,\mathrm{cm}^{-1}$ (dashed line in Fig. 2g) coincides with the steepest increase of the resistivity, i.e., the largest values of the exponent $\beta > 2$.

The emergence and fading of the DDP at T_{FL} and T_{BR}, respectively, indicate that the observed behavior is tightly linked to the bad-metal response in the resistivity, tracking the changes experienced by the QPs as the Fermi liquid degrades. This physical picture is reminiscent of the recently introduced concept[9–11] of 'resilient' QPs, which persist beyond the nominal Fermi-liquid regime, but with modified (e.g., T-dependent) QP parameters. Note that the DDP phenomenon observed here, that is not predicted by current theoretical descriptions of Mott systems[9,33], also impacts charge transport itself: for example, the values of σ_1 and γ seen at finite frequency in our optical experiments, which yield correlation strengths $U/W = 1.3$ for $x \geq 0.28$ (see Supplementary Fig. 6), are compatible with those computed by DMFT[33], but the measured dc resistivity increases way beyond the theory values — a natural consequence of the drop of σ_1 at low frequencies upon DDP formation.

Building on the considerations above, we now show that our experimental observations can be explained by an incipient localization of the carriers in the bad metal, caused by non-local, coherent backscattering corrections to semi-classical transport[34,35]. We note that related ideas have been invoked to explain the bad metallicity and DDP observed in liquid metals[34] and various correlated systems, including organics[36], cuprates[37,38], and other oxides[39], but no systematic quantitative investigations have been provided to date.

In order to describe the experimental observations, we now introduce a model that assigns the modifications of the Drude peak to backscattering processes[34,35,40,41]:

$$\sigma(\omega) = \frac{\epsilon_0 \omega_p^2}{\gamma - \gamma_b} \left[\frac{\gamma}{\gamma - i\omega} - \frac{\gamma_b}{\gamma_b - i\omega} \right]. \quad (2)$$

Here the first term between brackets represents the standard metallic response with the energy-dependent γ from Eq. (1), where ω_p is the plasma frequency. The second term represents the leading finite-frequency correction beyond semiclassical transport, caused by additional elastic or quasi-elastic processes. Its sign is opposite to that of the semiclassical Drude response, leading to a dip-peak structure in $\sigma_1(\omega)$ as illustrated in the inset of Fig. 1. The resulting peak frequency, $\omega_{peak} \simeq \sqrt{\gamma(0)\gamma_b}$, gives a direct measure of the backscattering rate γ_b. Physically, the "localization" corrections embodied in Eq. (2) represent non-local interference processes, which can be viewed as finite-frequency precursors of a disorder-induced bound-state formation.

We have used Eq. (2) to fit the finite-frequency spectra at the substitution $x = 0.28$, where the DDP is most clearly identified in the experiment. The Fermi-liquid response has been extracted from Fig. 3, setting a constant $B = 6.7 \times 10^{-4}$ cm at all temperatures up to $T = 100$ K. Importantly, ω_p^2 is also kept constant, compatible with the fact that the spectral weight associated with the QPs is conserved from the Fermi liquid to the bad-metallic region. The fits accurately describe the experimental data, as demonstrated by magenta lines for $\sigma_1(T, \omega)$ in Fig. 4d–g and for $\gamma(T, \omega)$ in Fig. 3a, b. Similar to the direct determination from the extended Drude analysis, the extracted $\gamma(0)$ shows an initial T^2 dependence which is lost at $T \geq T_{FL}$, as illustrated in Fig. 4i. The parameter $\gamma_b \ll \gamma(0)$ shows a similar trend.

To get further microscopic insight, we isolate explicitly the anomalous scattering contributions by writing

$$\delta\gamma(\omega, T) = \gamma(\omega, T) - \gamma_{FL,2}(\omega, T), \quad (3)$$

where $\gamma(\omega, T)$ is the measured scattering rate, which has the general form Eq. (1), and $\gamma_{FL,2}$ is the strict Fermi-liquid prediction, i.e., Eq. (1) with $p = 2$. Direct comparison with Eq. (1) yields $\delta\gamma(\omega, T) = B(p^2 - 2^2)(\pi k_B T/\hbar)^2$, from which the following conclusions can be drawn. First, the fact that we find a frequency-independent correction directly confirms the assumed (quasi)static nature of the anomalous scatterers. Second, the fact that $p = 6 \pm 1$ is almost constant for all substitutions (Fig. 3c, inset) means that the strength of $\delta\gamma$ (in particular its variation with x) is governed by the QP scale embodied in the parameter B, i.e., $\delta\gamma \sim \left(\frac{m^*}{m_b}\right)^2 \sim Z^{-2}$. This observation stresses the key role of strong correlation effects in the vicinity of the Mott point. Third, $p \gg 2$ implies that the anomalous contribution $\delta\gamma$ is dominant over the inelastic term, which consistently ensures that the corresponding localization effects are robust against the dephasing effects originating from inelastic QP scattering: whenever observed, the peak frequency ω_{peak} is much larger than the calculated dephasing term, $\sim B\omega^2$.

Discussion

The κ-[(BEDT-STF)$_x$(BEDT-TTF)$_{1-x}$]$_2$Cu$_2$(CN)$_3$ series studied here realizes a continuous tuning through the genuine Mott MIT near $T \to 0$ that was previously not accessible by experiments applying physical pressure. Our systematic investigation of the electron liquid from the weakly interacting limit to the Mott insulator establishes Landau's QPs as the relevant low-energy excitations throughout the metallic phase. While demonstrating the universality of Landau's QP picture, the foregoing analysis also reveals an enhanced elastic scattering channel that fundamentally alters the QP properties in these materials. This is best visible within the bad-metallic regime, where it conspires with electronic correlations in causing a progressive shift of the Drude peak to finite frequencies, indicative of dynamical localization of the QPs. Our analysis also suggests that the same elastic processes may already set in within the Fermi-liquid regime, causing deviations from the predicted ω^2/T^2 scaling laws of QP relaxation. These conclusions are largely based on a straightforward analysis of experimental data by a general theoretical model describing the optical response of charge carriers in the presence of incipient localization. We now discuss possible scenarios to elucidate the possible microscopic origins. The key feature that requires explanation is the pronounced elastic scattering near the Mott point.

One firmly established example leading to DDP behavior and anomalously high resistivities is the "transient localization" phenomenon found in crystalline organic semiconductors[42]. There, soft lattice fluctuations provide a strong source of quasi-elastic randomness at room temperature, causing coherent backscattering at low frequency and DDPs[41,43]. In the present κ-STF$_x$ compounds the Debye temperature for the relevant inter-molecular phonons, $T_D \sim 30K$, is similar to that of organic semiconductors, compatible with transient localization at high T. However, this picture is difficult to reconcile with the observed DDP at very low T close to the MIT that exhibits strong substitution dependence, indicating instead a clear connection with the Mott phenomenon. Similar caveats would apply if lattice fluctuations were replaced by other soft bosons unrelated to the Mott MIT, such as charge/magnetic collective modes. While the latter can also give rise to finite-frequency absorption peaks, our clear assignment of the DDP to metallic QP rules out such a situation in the present case[44,45].

An alternative possibility, that could reconcile the different experimental observations, is the physical picture of weakly disordered Fermi liquids[46,47], motivated by the unavoidable structural disorder that accompanies chemical substitution[16]. Although a complete theory for such a situation is still not available, existing studies[47] show that disorder directly affects the Fermi liquid, making its coherence scale T_{BR} spatially inhomogeneous with a broad distribution of local QP weights. In this case, one expects local regions with low T_{FL} to 'drop out' from the Fermi liquid and thus act essentially as vacancies — dramatically increasing the elastic scattering as temperature is raised.

While providing a plausible physical picture for $p > 2$, this scenario would also be consistent with the observed scaling of γ with $\left(\frac{m^\star}{m_b}\right)^2$ upon approaching the Mott point, reflecting the gradual build-up of correlations in the disordered Fermi liquid.

Finally, we argue that long-range Coulomb interactions, that are usually neglected in theoretical treatments of correlated electron systems, could actually play a key role both in the present compounds as well as in other bad metals where DDPs have been reported[45]. The ability of non-local interactions in providing an effective disordered medium for lattice electrons has been recognized recently[48–51], with direct consequences on bad-metallic behavior[52]. The additional scattering channel associated with long-range potentials could well be amplified at the approach of the Mott transition, due to both reduced screening and collective slowing down of the resulting randomness, possibly causing DDP behavior as observed here.

Since the gradual demise of quasiparticles is a general phenomenon in poor conductors, displaced Drude peaks likely occur in many of them[45]. In light of the present experiments, studying the interplay between electronic correlations and (self-induced) randomness appears to be a very promising route for understanding how good metals turn bad.

Methods

Experimental. Plate-like single crystals of κ-[(BEDT-STF)$_x$(BEDT-TTF)$_{1-x}$]$_2$ Cu$_2$(CN)$_3$ were grown electrochemically[16] with a typical size of $1 \times 1 \times 0.3$ mm^3; here BEDT-TTF stands for bis(ethylenedithio)tetrathiafulvalene and BEDT-STF denotes the partial substitution by selenium according to Fig. 2a. The composition of $0 \leq x \leq 1$ was determined by energy-dispersive X-ray spectroscopy[16]. The dc resistivity was recorded by standard four-point measurements; superconductivity was probed by magnetic susceptibility studies of polycrystalline samples using a commercial SQUID and magnetoresistance measurements on single crystals. We performed complementary pressure-dependent transport experiments of the parent compound ($x = 0$), shown in Supplementary Fig. 2b, providing the gray data points in Fig. 4a. Since the compounds are isostructural, they retain the highly frustrated triangular lattice and do not exhibit magnetic order down to lowest temperatures; a hallmark of the spin-liquid state. Using Fourier-transform infrared spectroscopy, the optical reflectivity at normal incidence was measured in the frequency range from 50 to 20000 cm^{-1} from $T = 5$ K up to room temperature; here also the visible and ultraviolet regimes were covered up to 47,600 cm^{-1} by a Woollam ellipsometer. The complex optical conductivity $\hat{\sigma}(\omega) = \sigma_1(\omega) + i\sigma_2(\omega)$ is obtained via the Kramers–Kronig relations using standard extrapolations. Since the optical properties of both crystal axes provide similar information, we focus on the spectra acquired for the polarization along the crystallographic c-axis.

Extended drude analysis. The frequency-dependent scattering rate and effective mass are calculated via the extended Drude model[53,54]

$$\gamma(\omega) = \epsilon_0 \omega_p^2 \, \mathrm{Re}\left\{[\hat{\sigma}(\omega)]^{-1}\right\} \tag{4}$$

$$\frac{m^\star(\omega)}{m_b} = \frac{\epsilon_0 \omega_p^2}{\omega} \, \mathrm{Im}\left\{-[\hat{\sigma}(\omega)]^{-1}\right\}, \tag{5}$$

where $\omega_p = \sqrt{Ne^2/\epsilon_0 m_b}$ is the plasma frequency, comprising the charge-carrier density N and band mass m_b; ϵ_0 is the permittivity of vacuum and e the elementary charge. ω_p is determined from the maximum of the dielectric loss function around 4000 cm^{-1} (see Supplementary Fig. 9).

Data availability

The authors declare that the data supporting the findings of this study are available within the paper and its Supplementary Information. Further information can be provided by A.P., M.D., or S.F.

References

1. Landau, L. D. The theory of a Fermi liquid. *Zh. Eksp. Teor. Fiz.* **30**, 1058 (1956).

2. Gurzhi, R. Mutual electron correlations in metal optics. *J. Exp. Theor. Phys.* **8**, 673 (1959).

3. Maslov, D. L. & Chubukov, A. V. First-Matsubara-frequency rule in a Fermi liquid. II. Optical conductivity and comparison to experiment. *Phys. Rev. B* **86**, 155137 (2012).

4. Berthod, C. et al. Non-Drude universal scaling laws for the optical response of local Fermi liquids. *Phys. Rev. B* **87**, 115109 (2013).

5. Maslov, D. L. & Chubukov, A. V. Optical response of correlated electron systems. *Rep. Prog. Phys.* **80**, 026503 (2017).

6. Gunnarsson, O., Calandra, M. & Han, J. E. Colloquium: saturation of electrical resistivity. *Rev. Mod. Phys.* **75**, 1085–1099 (2003).

7. Hussey, N. E., Takenaka, K. & Takagi, H. Universality of the Mott-Ioffe-Regel limit in metals. *Philos. Mag.* **84**, 2847–2864 (2004).

8. Georges, A., Kotliar, G., Krauth, W. & Rozenberg, M. J. Dynamical mean-field theory of strongly correlated fermion systems and the limit of infinite dimensions. *Rev. Mod. Phys.* **68**, 13–125 (1996).

9. Deng, X. et al. How bad metals turn good: spectroscopic signatures of resilient quasiparticles. *Phys. Rev. Lett.* **110**, 086401 (2013).

10. Milbradt, S. et al. In-plane superfluid density and microwave conductivity of the organic superconductor κ-(BEDT-TTF)$_2$Cu[N(CN)$_2$]Br: evidence for d-wave pairing and resilient quasiparticles. *Phys. Rev. B* **88**, 064501 (2013).

11. Deng, X., Sternbach, A., Haule, K., Basov, D. N. & Kotliar, G. Shining light on transition-metal oxides: unveiling the hidden Fermi liquid. *Phys. Rev. Lett.* **113**, 246404 (2014).

12. Hartnoll, S. A. Theory of universal incoherent metallic transport. *Nat. Phys.* **11**, 54–61 (2015).

13. Pustogow, A. et al. Quantum spin liquids unveil the genuine Mott state. *Nat. Mater.* **17**, 773–777 (2018).

14. Dressel, M. & Pustogow, A. Electrodynamics of quantum spin liquids. *J. Phys. Condens. Matter* **30**, 203001 (2018).

15. Shimizu, Y., Miyagawa, K., Kanoda, K., Maesato, M. & Saito, G. Spin liquid state in an organic Mott insulator with a triangular lattice. *Phys. Rev. Lett.* **91**, 107001 (2003).

16. Saito, Y., Minamidate, T., Kawamoto, A., Matsunaga, N. & Nomura, K. Site-specific ^{13}C NMR study on the locally distorted triangular lattice of the organic conductor κ-(BEDT-TTF)$_2$Cu$_2$(CN)$_3$. *Phys. Rev. B* **98**, 205141 (2018).

17. Kurosaki, Y., Shimizu, Y., Miyagawa, K., Kanoda, K. & Saito, G. Mott transition from a spin liquid to a Fermi liquid in the spin-frustrated organic conductor κ-(ET)$_2$Cu$_2$(CN)$_3$. *Phys. Rev. Lett.* **95**, 177001 (2005).

18. Furukawa, T., Miyagawa, K., Taniguchi, H., Kato, R. & Kanoda, K. Quantum criticality of Mott transition in organic materials. *Nat. Phys.* **11**, 221–224 (2015).

19. Furukawa, T., Kobashi, K., Kurosaki, Y., Miyagawa, K. & Kanoda, K. Quasi-continuous transition from a Fermi liquid to a spin liquid in κ-(ET)$_2$Cu$_2$(CN)$_3$. *Nat. Commun.* **9**, 307 (2018).

20. Jacko, A. C., Fjaerestad, J. O. & Powell, B. J. A unified explanation of the Kadowaki–Woods ratio in strongly correlated metals. *Nat. Phys.* **5**, 422–425 (2009).

21. Vučičević, J., Terletska, H., Tanasković, D. & Dobrosavljević, V. Finite-temperature crossover and the quantum Widom line near the Mott transition. *Phys. Rev. B* **88**, 075143 (2013).

22. Brinkman, W. F. & Rice, T. M. Application of Gutzwiller's variational method to the metal-insulator transition. *Phys. Rev. B* **2**, 4302–4304 (1970).

23. Radonjić, M. M., Tanasković, D., Dobrosavljević, V., Haule, K. & Kotliar, G. Wigner-Mott scaling of transport near the two-dimensional metal-insulator transition. *Phys. Rev. B* **85**, 085133 (2012).

24. Pustogow, A. et al. Low-temperature dielectric anomaly arising from electronic phase separation at the Mott insulator-metal transition. *NPJ Quantum Mater.* **6**, 9 (2021).

25. Terletska, H., Vučičević, J., Tanasković, D. & Dobrosavljević, V. Quantum critical transport near the Mott transition. *Phys. Rev. Lett.* **107**, 026401 (2011).

26. Tytarenko, A., Huang, Y., de Visser, A., Johnston, S. & van Heumen, E. Direct observation of a Fermi liquid-like normal state in an iron-pnictide superconductor. *Sci. Rep.* **5**, 012421 (2015).

27. Nagel, U. et al. Optical spectroscopy shows that the normal state of URu$_2$Si$_2$ is an anomalous Fermi liquid. *Proc. Natl. Acad. Sci.* **109**, 19161–19165 (2012).

28. Mirzaei, S. I. et al. Spectroscopic evidence for Fermi liquid-like energy and temperature dependence of the relaxation rate in the pseudogap phase of the cuprates. *Proc. Natl. Acad. Sci.* **110**, 5774 (2013).

29. Stricker, D. et al. Optical response of Sr$_2$RuO$_4$ reveals universal Fermi-liquid scaling and quasiparticles beyond Landau theory. *Phys. Rev. Lett.* **113**, 087404 (2014).

30. Yasin, S. et al. Transport studies at the Mott transition of the two-dimensional organic metal κ-(BEDT-TTF)$_2$Cu[N(CN)$_2$]Br$_x$Cl$_{1-x}$. *Eur. Phys. J. B* **79**, 383–390 (2011).

31. Senthil, T. Theory of a continuous Mott transition in two dimensions. *Phys. Rev. B* **78**, 045109 (2008).

32. Lee, T.-H., Florens, S. & Dobrosavljević, V. Fate of spinons at the Mott point. *Phys. Rev. Lett.* **117**, 136601 (2016).
33. Radonjić, M. M., Tanasković, D., Dobrosavljević, V. & Haule, K. Influence of disorder on incoherent transport near the Mott transition. *Phys. Rev. B* **81**, 075118 (2010).
34. Smith, N. V. Classical generalization of the Drude formula for the optical conductivity. *Phys. Rev. B* **64**, 155106 (2001).
35. Fratini, S., Mayou, D. & Ciuchi, S. The transient localization scenario for charge transport in crystalline organic materials. *Adv. Funct. Mater.* **26**, 2292–2315 (2016).
36. Takenaka, K. et al. Collapse of coherent quasiparticle states in θ-(BEDT-TTF)$_2$I$_3$ observed by optical spectroscopy. *Phys. Rev. Lett.* **95**, 227801 (2005).
37. Takenaka, K., Nohara, J., Shiozaki, R. & Sugai, S. Incoherent charge dynamics of La$_{2-x}$Sr$_x$CuO$_4$: dynamical localization and resistivity saturation. *Phys. Rev. B* **68**, 134501 (2003).
38. Hwang, J., Timusk, T. & Gu, G. D. Doping dependent optical properties of Bi$_2$Sr$_2$CaCu$_2$O$_{8+\delta}$. *J. Phys. Condens. Matter* **19**, 125208 (2007).
39. Kostic, P. et al. Non-Fermi-liquid behavior of SrRuO$_3$: evidence from infrared conductivity. *Phys. Rev. Lett.* **81**, 2498–2501 (1998).
40. Fratini, S., Ciuchi, S. & Mayou, D. Phenomenological model for charge dynamics and optical response of disordered systems: application to organic semiconductors. *Phys. Rev. B* **89**, 235201 (2014).
41. Fratini, S. & Ciuchi, S. Dynamical localization corrections to band transport. *Phys. Rev. Res.* **2**, 013001 (2020).
42. Fratini, S., Nikolka, M., Salleo, A., Schweicher, G. & Sirringhaus, H. Charge transport in high-mobility conjugated polymers and molecular semiconductors. *Nat. Mater.* https://doi.org/10.1038/s41563-020-0647-2 (2020).
43. Schubert, G., Wellein, G., Weisse, A., Alvermann, A. & Fehske, H. Optical absorption and activated transport in polaronic systems. *Phys. Rev. B* **72**, 104304 (2005).
44. Caprara, S., Di Castro, C., Fratini, S. & Grilli, M. Anomalous optical absorption in the normal state of overdoped cuprates near the charge-ordering instability. *Phys. Rev. Lett.* **88**, 147001 (2002).
45. Delacrétaz, L., Goutéraux, B., Hartnoll, S. & Karlsson, A. Bad metals from fluctuating density waves. *SciPost Phys.* **3**, 25 (2017).
46. Aguiar, M. C. O., Dobrosavljević, V., Abrahams, E. & Kotliar, G. Effects of disorder on the non-zero temperature Mott transition. *Phys. Rev. B* **71**, 205115 (2005).
47. Andrade, E. C., Miranda, E. & Dobrosavljević, V. Electronic Griffiths phase of the $d=2$ Mott transition. *Phys. Rev. Lett.* **102**, 206403 (2009).
48. Pramudya, Y., Terletska, H., Pankov, S., Manousakis, E. & Dobrosavljević, V. Nearly frozen Coulomb liquids. *Phys. Rev. B* **84**, 125120 (2011).
49. Mahmoudian, S., Rademaker, L., Ralko, A., Fratini, S. & Dobrosavljević, V. Glassy dynamics in geometrically frustrated Coulomb liquids without disorder. *Phys. Rev. Lett.* **115**, 025701 (2015).
50. Rademaker, L., Ralko, A., Fratini, S. & Dobrosavljević, V. Avoiding stripe order: emergence of the supercooled electron liquid. *J. Supercond. Nov. Magn.* **29**, 601–604 (2016).
51. Driscoll, K., Ralko, A. & Fratini, S. Pseudogap metal induced by long-range Coulomb interactions Preprint at https://arxiv.org/abs/2010.02858 (2020).
52. Mousatov, C. H., Esterlis, I. & Hartnoll, S. A. Bad metallic transport in a modified Hubbard model. *Phys. Rev. Lett.* **122**, 186601 (2019).
53. Allen, J. W. & Mikkelsen, J. C. Optical properties of CrSb, MnSb, NiSb, and NiAs. *Phys.Rev. B* **15**, 2952–2960 (1977).
54. Dressel, M. & Grüner, G. *Electrodynamics of Solids: Optical Properties of Electrons in Matter* (Cambridge University Press: 2002).

Author contributions
A.P. and M.D. guided and conceived the experimental work. Optical experiments were conducted by A.P. and M.S.A., supported by Y.S. Dc transport measurements were performed by Y.S. and A.L. Crystals were grown by Y.S. and A.K. Circumstantial analysis of all results was carried out by A.P., with support from S.F. and in exchange with V.D. and M.D. Theoretical work was performed by S.F., with contributions from V.D. A.P., V.D., M.D., and S.F. discussed the data, interpreted the results, and wrote the paper with input from all authors.

Competing interests
The authors declare no competing interests.

Additional information
Supplementary information The online version contains supplementary material available at https://doi.org/10.1038/s41467-021-21741-z.

Correspondence and requests for materials should be addressed to A.P., M.D. or S.F.

Peer review information *Nature Communications* thanks Benjamin Powell and the other, anonymous, reviewer(s) for their contribution to the peer review of this work.

Reprints and permission information is available at http://www.nature.com/reprints

Publisher's note Springer Nature remains neutral with regard to jurisdictional claims in published maps and institutional affiliations.

Rise and Fall of Landau's Quasiparticles While Approaching the Mott Transition

A. Pustogow⋆,[1,2] Y. Saito,[1,3] A. Löhle,[1] M. Sanz Alonso,[1] A.

Kawamoto,[3] V. Dobrosavljević,[4] M. Dressel,[1] and S. Fratini[5]

[1]1. Physikalisches Institut, Universität Stuttgart, 70569 Stuttgart, Germany

[2]Department of Physics and Astronomy, UCLA, Los Angeles, California 90095, USA

[3]Department of Physics, Graduate School of Science, Hokkaido University, Sapporo 060-0810, Japan

[4]Department of Physics and National High Magnetic Field Laboratory,

Florida State University, Tallahassee, Florida 32306, USA

[5]Institut Néel - CNRS and Université Grenoble Alpes, 38042 Grenoble Cedex 9, France
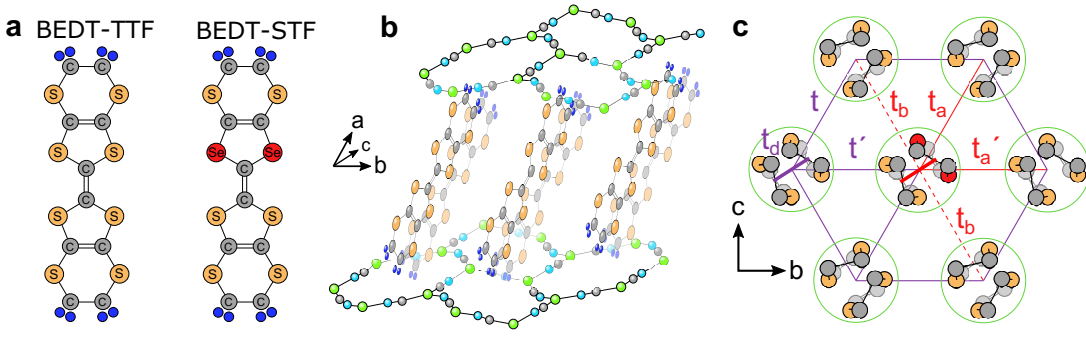
(Dated: January 20, 2021)

CONTENTS

SUPPLEMENTARY NOTE 1: CRYSTAL STRUCTURE

Single crystals of κ-[(BEDT-STF)$_x$(BEDT-TTF)$_{1-x}$]$_2$Cu$_2$(CN)$_3$ with the stoichiometries $x = 0$, 0.04, 0.1, 0.12, 0.16, 0.19, 0.21, 0.25, 0.28, 0.44, 0.78 and 1.00 were prepared by standard electrochemical oxidation [1]. BEDT-TTF stands for bis(ethylenedithio)tetrathiafulvalene and BEDT-STF for bis-(ethylenedithio)diselenium-dithiafulvalene. While BEDT-TTF molecules were purchased from Sigma-Aldrich, the synthesis of BEDT-STF and the crystal growth were carried out at Hokkaido University in Sapporo. The two types of molecules are displayed in Supplementary Fig. 1a. In order to create different substitutions in the alloy series, the amount of donor molecules was preselected; the actual value x was determined *a posteriori* by energy-dispersive x-ray spectroscopy for each batch: we compared the intensity of S atoms to that of Se atoms, using κ-(BEDT-TTF)$_2$Cu$_2$(CN)$_3$ as a reference. More information on crystal growth can be found in Supplementary Ref. 2.
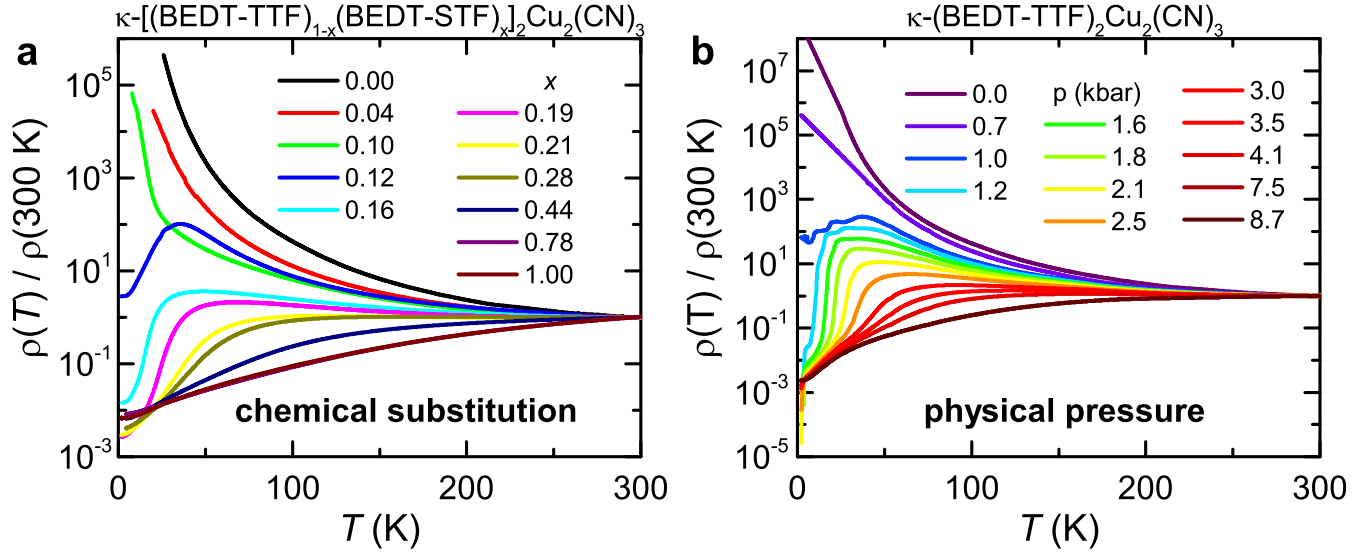

⋆Present Address: Institute of Solid State Physics, Vienna University of Technology, 1040 Vienna, Austria.

Supplementary Figure 1. **Crystal structure. a,** Organic donor molecules BEDT-TTF and BEDT-STF. For the latter, two of the inner sulfur atoms are substituted by selenium. **b,** The crystal structure consists of layers of the donor molecules along the bc-plane that are separated by the polymeric $Cu_2(CN)_3$ anion network. **c,** Within the layers, the BEDT-TTF (BEDT-STF) dimers form a slightly anisotropic triangular arrangement with transfer integrals $t'/t = 0.83$ [3], i.e. the lattice is subject to significant geometrical frustration. Substitution of BEDT-TTF by BEDT-STF enlarges the transfer integrals (red) due to the extended orbitals of the selenium-containing BEDT-STF molecules. Note, also the intra-dimer transfer integrals, $t_d \gg t, t'$, are enhanced by substitution.
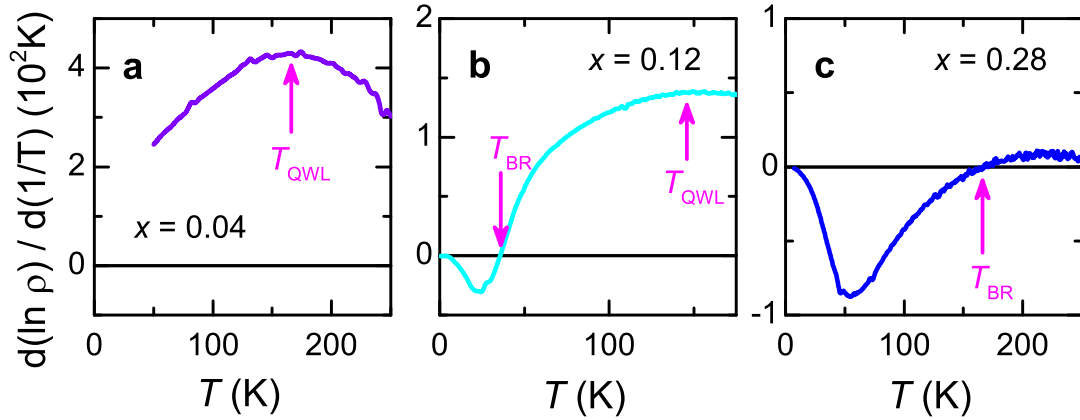
The BEDT-TTF (resp. BEDT-STF) molecules form dimers because the intra-dimer transfer integral t_d is significantly larger than the inter-dimer wave function overlaps t and t' (Supplementary Fig. 1c). Per dimer one electron is donated to the $[Cu_2(CN)_3]_\infty^-$ anion sheets that separate the donor layers as shown in Supplementary Fig. 1b. Within the bc plane the dimers constitute a slightly anisotropic triangular lattice that is close to ideal geometrical frustration, $t'/t = 0.83$ [3] as illustrated in Supplementary Fig. 1c. The system is subject to strong electronic correlations as, overall, each dimer carries one hole with spin 1/2: on-site Coulomb repulsion among the charges realizes a Mott insulator at half filling [4]. In the alloys the BEDT-TTF molecules are randomly substituted by BEDT-STF, which mainly leads to an increase of the electronic bandwidth. It may also give rise to disorder in the transfer integrals, similar to chemical substitution or doping in other materials.

SUPPLEMENTARY NOTE 2: DC RESISTIVITY

Standard four-point dc transport experiments were carried out for the alloy series κ-$[(BEDT-STF)_x(BEDT-TTF)_{1-x}]_2Cu_2(CN)_3$ in the temperature range from $T = 300$ K down to 2 K. Supplementary Fig. 2a shows the complete set of resistivity curves $\rho(T)$ normalized to 300 K that were used to construct the phase diagrams in Fig. 2d and Fig. 4a. Prior to performing the logarithmic derivative, the residual resistivity ρ_0 in the limit $T \to 0$ has to be subtracted in order to yield the power-law exponent $\beta = d(\ln\{\rho - \rho_0\})/d(\ln\{T\})$. While the Fermi-liquid temperature T_{FL} is reached when the resistivity deviates from $\rho(T) = \rho_0 + AT^2$, the Brinkman-Rice temperature T_{BR} is defined when $\rho(T)$ goes through a maximum; both temperatures are indicated in Fig. 2. In Supplementary Fig. 3a,b we illustrate how the quantum Widom line is determined: the steepest slope in the Arrhenius plot corresponds to the maximum in $d(\ln\{\rho\})/d(1/T)$; this is the distinctive criterion for T_{QWL} (cf. Fig. S2 in Supplementary Ref. 9). As seen in Supplementary Fig. 2a, a Mott-insulating behavior occurs only for $x \leq 0.12$. The larger substitutions ($x \geq 0.12$) behave metallic below T_{BR}; this corresponds to a sign change in $d(\ln\{\rho\})/d(1/T)$ as seen in Supplementary Fig. 3b,c. Furthermore for κ-$[(BEDT-STF)_x(BEDT-TTF)_{1-x}]_2Cu_2(CN)_3$ with $x = 0.10$ and 0.12 we find that around 2.5 - 3 K superconductivity sets in at ambient pressure.

Supplementary Figure 2. **Substitutional and pressure evolution of the dc resistivity. a,** The temperature dependence of the dc resistivity (normalized to $T = 295$ K) is plotted for the series κ-[(BEDT-STF)$_x$(BEDT-TTF)$_{1-x}$]$_2$Cu$_2$(CN)$_3$ [5]. **b,** Temperature-dependent dc resistivity was measured on κ-(BEDT-TTF)$_2$Cu$_2$(CN)$_3$ for increasing hydrostatic pressure. The resistivity $\rho(T)$ is successively reduced with higher pressure: metallic behavior and superconductivity are observed at low temperatures, in agreement with literature [6–8]. The pressure values indicated here correspond to the lowest temperature. During cooling the pressure is reduced due to thermal contraction and freezing of the pressure-transmitting medium (Daphne oil). *In-situ* calibration allows us to determine the actual pressure at each temperature, which is taken into account in Fig. 3a.

Supplementary Figure 3. **Transport gap defines quantum Widom line. a,b,** For those compounds that show Mott-insulating behavior, $x = 0.04$ and $x = 0.12$, a maximum in the logarithmic derivative indicates the temperature when $\rho(T)$ crosses the quantum Widom line. **b,c,** The change of sign defines the Brinkman-Rice temperature T_{BR} as the onset of metallic transport $(d(\ln \rho)/d(1/T) < 0)$.
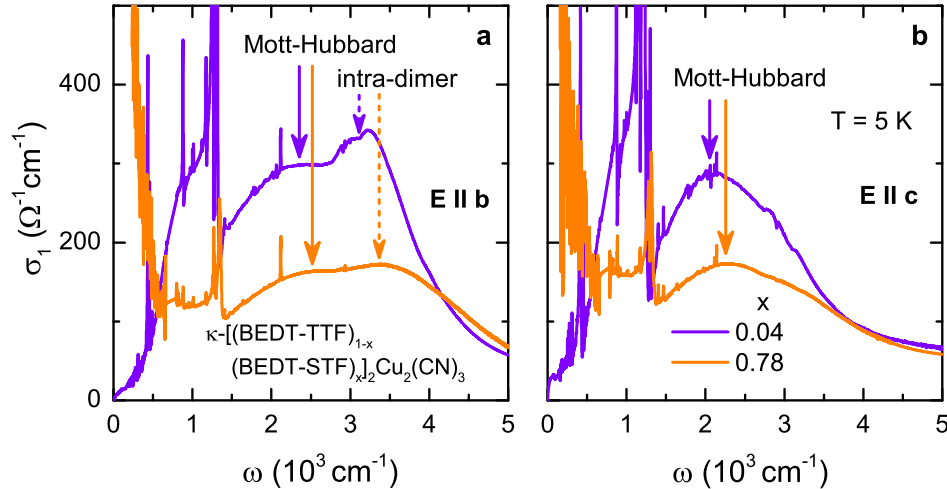
In addition to ambient-pressure dc transport experiments on the κ-[(BEDT-STF)$_x$(BEDT-TTF)$_{1-x}$]$_2$Cu$_2$(CN)$_3$ alloy series, we performed complementary pressure-dependent resistivity measurements on the parent compound ($x = 0$); the results are displayed in Supplementary Fig. 2b. Here the Mott insulator-metal transition occurs slightly above 1 kbar and is accompanied by superconductivity (onset at $T_{c,max} \approx 5$ K), in agreement with previous work [6–8]. The resulting values for T_{QWL}, T_{FL}, T_{BR} and T_c are included in Fig. 4a; they line up well with the transition and crossover temperatures obtained via chemical substitution.
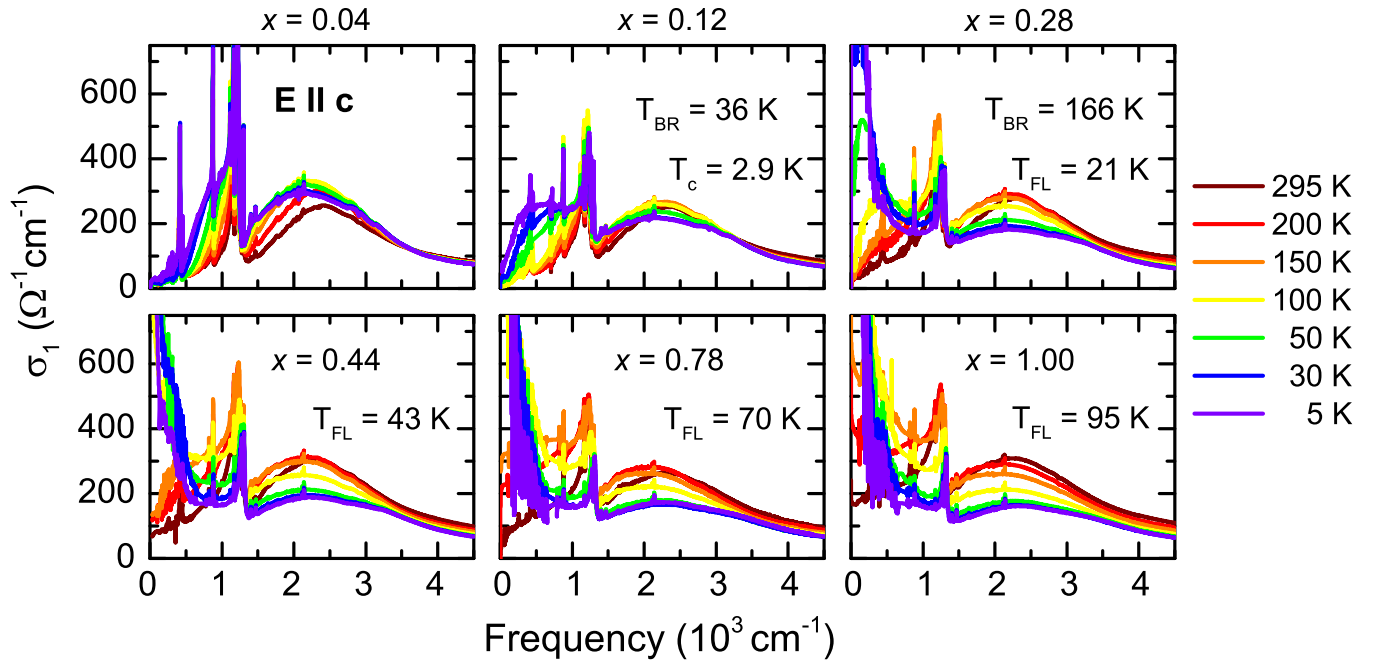
SUPPLEMENTARY NOTE 3: OPTICAL SPECTROSCOPY

Optical spectroscopic experiments were performed on the substitution series κ-[(BEDT-STF)$_x$(BEDT-TTF)$_{1-x}$]$_2$-Cu$_2$(CN)$_3$ covering a frequency range of 50–20000 cm^{-1} and for temperatures from 5 K up to 295 K. Due to the small in-plane anisotropy of the transfer integrals (Supplementary Fig. 1c), the dc resistivity differs by a factor 2 between the b and c directions [10]. In Supplementary Fig. 4 we compare the optical spectra of the two crystal axes. While for both polarizations the absorption exhibits a peak around 2500 cm^{-1} and 2000 cm^{-1}, respectively, along b-direction one can distinguish another feature above 3000 cm^{-1} which corresponds to intra-dimer excitations that do not contribute to charge transport [11–14]. Apart from minor quantitative differences, metallic and insulating behavior expresses for both in-plane axes as exemplarily shown here for the substitutions $x = 0.04$ and 0.78 in Supplementary Fig. 4. For the determination of U and W from the Mott-Hubbard transitions, we focused on the optical spectra acquired for $E \parallel c$.

In addition, a strong vibrational mode occurs around 1400 cm^{-1} related to intramolecular vibrations mainly involving C=C. Due to electron-molecular vibrational coupling, this feature can become rather intense and acquire an asymmetric Fano shape, in particular for in the insulating regime [15]. Although these vibrational features might appear disturbing, we refrain from subtracting them off the spectra in an arbitrary fashion; instead we present raw data whenever possible.
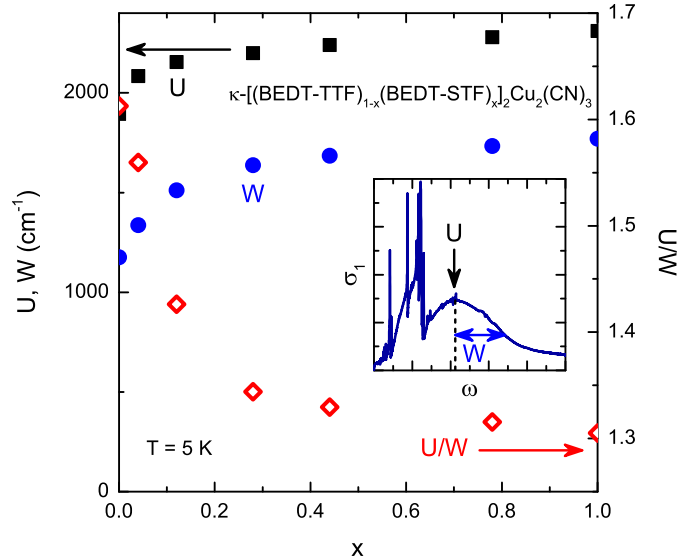
Supplementary Fig. 5 displays the full set of optical data ($x = 0.04, 0.12, 0.28, 0.44, 0.78, 1.00$; 5 K $< T <$ 295 K) of the alloying series discussed in the present work. Similar to the parent compound [16, 17], the substitution $x = 0.04$ exhibits an insulating-like optical conductivity with $\sigma_1(\omega \to 0) \to 0$ and $d\sigma_1/d\omega > 0$ below the Hubbard transitions at all temperatures. Also for $x = 0.12$ and 0.28, the high-temperature spectra ($T > T_{\mathrm{BR}}$) reveal insulating, or rather semiconducting properties – at finite temperature there is always a non-zero offset to σ_1 at $\omega = 0$ due to thermal

Supplementary Figure 4. **In-plane anisotropy.** The anisotropy of the in-plane electrodynamic response of κ-[(BEDT-STF)$_x$(BEDT-TTF)$_{1-x}$]$_2$Cu$_2$(CN)$_3$ between (a) $E \parallel b$ and (b) $E \parallel c$ is exemplified for $x = 0.04$ and 0.78 at $T = 5$ K. The main contribution along both crystal axes is due to Mott-Hubbard excitations between the dimers (solid arrows) [11–14]. Overall, the Coulomb repulsion U, associated with the band maximum, and the corresponding electronic correlation strength U/W are slightly larger for $E \parallel b$ [9]. Local intra-dimer excitations show up above 3000 cm^{-1} (dashed lines) and are more pronounced along the b-direction as compared to $E \parallel c$. Both electronic contributions shift to higher energy with increasing STF content x.
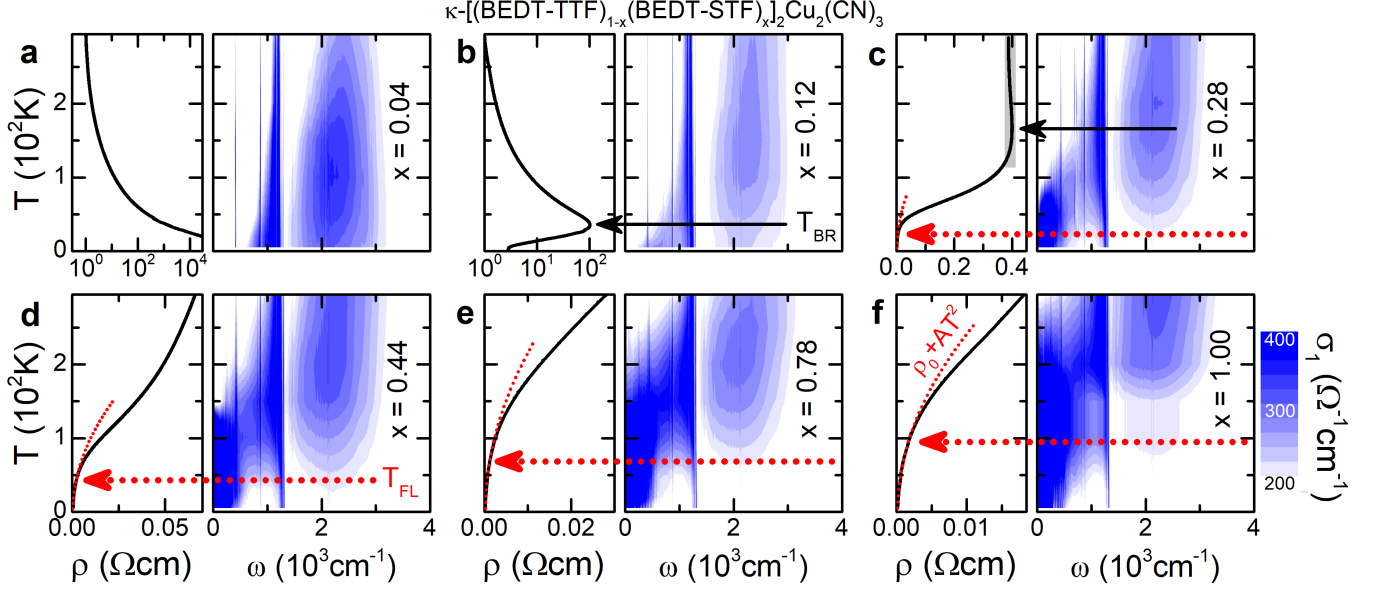
Supplementary Figure 5. **Temperature-dependent optical conductivity for all substitutions.** The optical conductivity of κ-[(BEDT-STF)$_x$(BEDT-TTF)$_{1-x}$]$_2$Cu$_2$(CN)$_3$ was determined in reflection experiments from room temperature down to $T = 5$ K. As substitution $x = 0.04, 0.12, 0.28, 0.44, 0.78, 1.00$ increases, spectral weight successively accumulates at low frequencies coincident with the onset of metallic behavior below T_{BR}. A Drude-like peak forms at zero frequency for $T < T_{FL}$.

Supplementary Figure 6. **Band parameters U, W and U/W of κ-STF$_x$.** The electronic bandwidth W and on-site Coulomb repulsion U were determined from the half-width at half maximum and the peak position, respectively. The increase of W is more pronounced for $x \to 1$ leading to an overall reduction of the correlation strength U/W (red symbols, right scale).

excitations across the gap. Below T_{BR}, however, a significant amount of the spectral weight accumulates at low frequencies. Eventually, a Drude-like peak is established at $\omega = 0$ for $T < T_{FL}$ in all substitutions $x \geq 0.28$ that contain Fermi-liquid properties in dc transport.
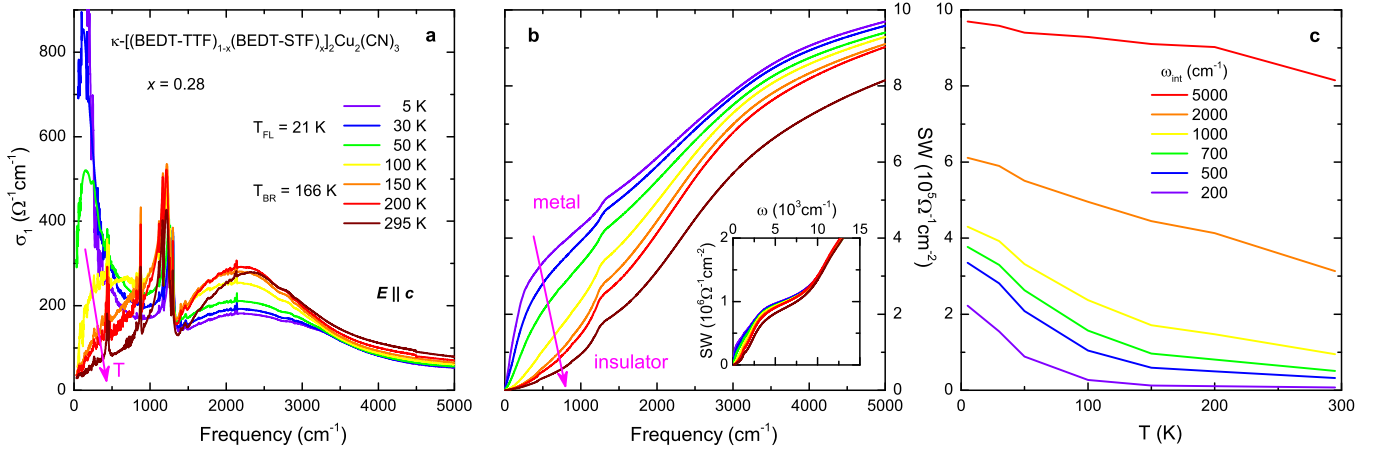
In Supplementary Fig. 6 we present the band parameters: the Coulomb repulsion U and the electronic bandwidth W

Supplementary Figure 7. **Temperature and frequency evolution of optical conductivity compared to dc resistivity in κ-STF$_x$. a,** The insulating compound with $x = 0.04$ exhibits an increase of the in-gap absorption upon cooling, despite monotonously increasing $\rho(T)$. Such non-thermal behavior of $\sigma_1(T,\omega)$ is also found in the parent compound ($x = 0$) and assigned to metallic fluctuations in the insulating state close to the metal-insulator transition [9]. **b,c,** Below T_{BR} a large part of the spectral weight separates from the Hubbard bands and gradually shifts to lower frequencies upon cooling, where it forms a metallic state at low temperatures. **c-f,** A well-defined quasiparticle peak forms at $T \leq T_{FL}$. The $\rho \propto T^2$ behavior (red dotted lines) is unanimously linked to a Drude-like response at $\omega = 0$, and the strong increase of resistivity in the bad metal arises from a successive spectral weight shift to finite frequencies upon warming. Metallic behavior is completely lost as the itinerant response merges with the Hubbard bands.

W are determined from the Mott-Hubbard transitions. As indicated in the inset, here we use the half-width at half-maximum on the high-frequency wing for a consistent determination of W because the appearance of the metallic component for the higher substitutions conceals the low-frequency side. The enhancement of W with increasing x substantiates that chemical substitution primarily tunes the bandwidth via the larger transfer integrals of the BEDT-STF molecules. In addition, also U increases, which we assign to the accompanying enlargement of the intra-dimer transfer integrals, that is empirically used to approximate the on-site term via $U \approx 2t_d$ [18, 19]. Overall, the enhancement of W is more pronounced than for U leading to a sizeable reduction of U/W with larger substitution, proving that the main effect of chemical substitution is tuning the bandwidth. This is in excellent agreement with the similarity of the Mott transition observed when applying physical pressure to κ-(BEDT-TTF)$_2$Cu$_2$(CN)$_3$ [6–8]; the results of both experiments are compared in Fig. 4a.

In order to relate the optical response of κ-[(BEDT-STF)$_x$(BEDT-TTF)$_{1-x}$]$_2$Cu$_2$(CN)$_3$ to their transport properties as a function of temperature, in Supplementary Fig. 7 we compare $\rho(T)$ with a false-color contour plot of $\sigma_1(T,\omega)$ for each substitution. For $x \geq 0.28$ one can clearly see that the concentration of optical conductivity around $\omega = 0$ coincides with the T^2-dependence of the resistivity (indicated by dotted red lines) in the Fermi-liquid state. Above T_{FL} the spectral weight associated with metallic quasiparticles gradually shifts to higher frequencies. Since around these temperatures the resistivity also exceeds the Ioffe-Regel-Mott (IRM) limit, the formation of a 'displaced Drude peak' (DDP) is clearly associated with the bad-metal phase. While a DDP was observed in a number of poor electrical conductors subject to pronounced electronic correlations [20], our results conclusively demonstrate that this

Supplementary Figure 8. **Spectral weight evolution for** $x = 0.28$. **a,** The optical conductivity of κ-[(BEDT-TTF)$_{0.72}$-(BEDT-STF)$_{0.28}$]$_2$Cu$_2$(CN)$_3$ is shown for all temperatures. **b,** The associated spectral weight (SW) clearly indicates the transition from a good metal at low temperatures to an insulating response above $T_{\mathrm{BR}} = 166$ K; in other words spectral weight shifts from low to high frequencies. Inset: for all temperatures the SW is conserved above $\omega \approx 10\,000$ cm^{-1}. **c,** Temperature dependence of the SW integrated up to several distinct cut-off frequencies ω_{int}, as indicated.

phenomenon emerges directly from a Fermi liquid and is, thus, comprised of quasiparticles. This nourishes the idea of 'resilient quasiparticles' discussed recently [21, 22].

The spectral weight shift from low to high frequencies above T_{FL} approximately follows a linear temperature dependence. In Supplementary Fig. 1 we estimated the temperature at which the DDP crosses $\omega = 100$ cm^{-1} (dashed black line) by following the T-ω trajectory of the peak position in the contour plots of Supplementary Fig. 7c-f. As the spectral contribution of itinerant carriers merges with the Hubbard excitations around 2000 cm^{-1}, the metallic properties get lost above T_{BR}, as seen in Supplementary Fig. 7b,c for $x = 0.12$ and 0.28. For the larger substitutions $x \geq 0.44$ this spectral feature broadens increasingly; and considerable weight remains at $\omega = 0$ retaining metallic transport properties. Note, even well above $T = 100$ K, the largest substitutions (Supplementary Fig. 7d-f) exhibit resistivities that deviate by less than a factor two from the low-temperature $\rho \propto T^2$ behavior. Naturally, this broad crossover from a Fermi liquid to a bad metal expresses similarly in $\sigma_1(\omega)$.

Finally, we point out that in Supplementary Fig. 7a-c a 'metallic-like' increase of the low-frequency spectral weight is also observed for $T > T_{\mathrm{BR}}$ where the resistivity exhibits insulating properties, i.e. $\mathrm{d}\rho/\mathrm{d}T < 0$ – even seen for the completely insulating compound with $x = 0.04$. In line with the discussion above, this contribution clearly originates from the metallic properties supporting our previous suggestion [9] that the 'non-thermal' increase of the low-energy spectral weight on the insulating side close to the Mott transition is associated to metallic fluctuations at finite frequencies. Overall, our optical results are in excellent agreement with dc transport, and provide information on the nature of metallic quasiparticles in the bad metal regime far beyond standard resistivity data.

In Supplementary Fig. 8a we exemplify the temperature dependence of the optical conductivity through the various conduction regimes for the example $x = 0.28$. While the 5 K-spectrum comprises a Drude-like peak centered at $\omega = 0$, at temperatures above $T_{\mathrm{FL}} = 21$ K a DDP can be clearly identified; here seen for $T = 30$, 50, and 100 K. As temperature increases, the spectral weight successively shifts to higher frequencies, as seen in the rising intensity around 2000–3000 cm^{-1}. The overall spectral weight, however, remains conserved for all temperatures around 10 000 cm^{-1}, above

which other types of excitations become dominant (Supplementary Fig. 8b inset). Panel c illustrates the temperature dependence of the spectral weight, when the integration is conducted from $\omega = 0$ up to different cut-off frequencies ω_{int}; we identify a strong increase below $T_{BR} = 166$ K as metallicity sets in. Clearly, the changes are most pronounced at the lowest frequencies, in particular when T_{FL} is approached.

SUPPLEMENTARY NOTE 4: EXTENDED DRUDE ANALYSIS

The extended Drude model [23, 24] assumes a frequency-dependent scattering rate $\gamma(\omega)$ and effective mass $m^{\star}(\omega)/m_b$. Both quantities are affected by electronic correlations via $Z < 1$ [25–27]. The complex optical conductivity $\hat{\sigma} = \sigma_1 + i\sigma_2$ of a correlated metal can be written as

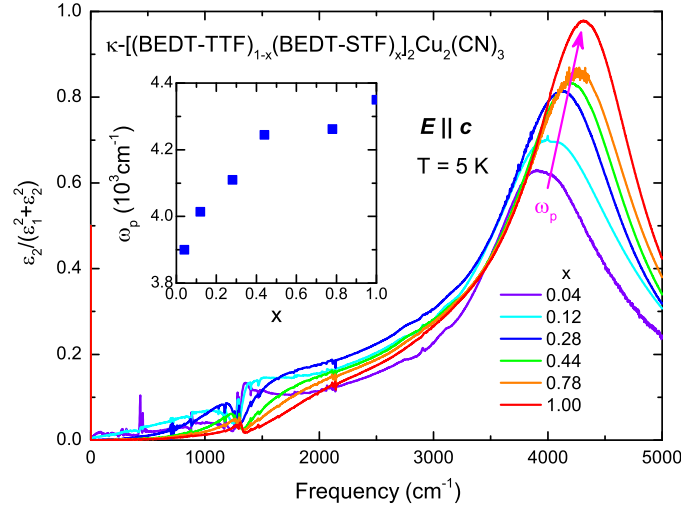$$\hat{\sigma}(\omega) = \frac{\epsilon_0 \omega_p^2}{\gamma} \frac{1}{1 + i\omega(m^{\star}/m_b)/\gamma}, \tag{1}$$

where $\omega_p = \sqrt{Ne^2/\epsilon_0 m_b}$ is the plasma frequency, reflecting the charge-carrier density N and band mass m_b; ϵ_0 is the permittivity of vacuum and e the elementary charge. Inversion of Supplementary Eq. 1 yields the frequency-dependent scattering rate and effective mass

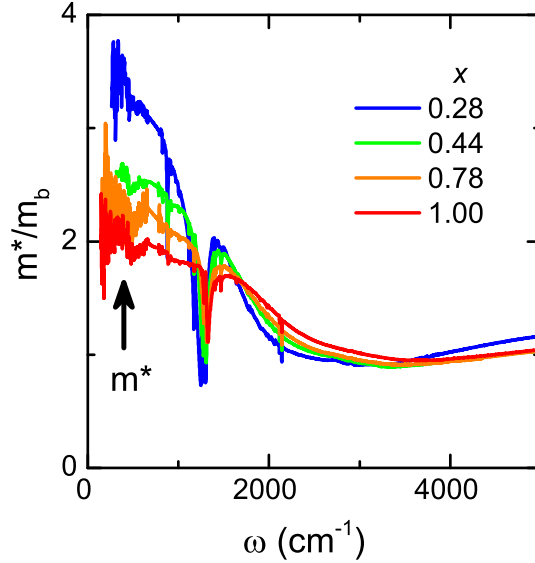$$\gamma(\omega) = \epsilon_0 \omega_p^2 \, \text{Re} \left\{ [\hat{\sigma}(\omega)]^{-1} \right\} \tag{2}$$

$$\frac{m^{\star}(\omega)}{m_b} = \frac{\epsilon_0 \omega_p^2}{\omega} \, \text{Im} \left\{ -[\hat{\sigma}(\omega)]^{-1} \right\} \quad . \tag{3}$$

The high-energy contributions are summarized as ϵ_∞, which commonly is subtracted from the real part of the complex dielectric constant $\hat{\epsilon} = \epsilon_1 + i\epsilon_2$ before the extended-Drude analysis can be performed [28]. The particular values of ϵ_∞ range from 2.75 to 3.04 for $x = 0.28$ - 1.00. The plasma frequency ω_p of the conduction electrons in Eqs. (2) and (3) is obtained from the peak of the dielectric loss function $-\text{Im} \left\{ \hat{\epsilon}^{-1} \right\} = \epsilon_2/(\epsilon_1^2 + \epsilon_2^2)$, which occurs slightly above 4000 cm^{-1} for the compounds that exhibit metallic transport properties, displayed in Supplementary Fig. 9.

In Supplementary Fig. 10, we plot the effective mass normalized to the band mass, $m^{\star}/m_b$, determined at the lowest measured temperature ($T = 5$ K) for the four compounds that exhibit Fermi-liquid properties, $x = 0.28$, 0.44, 0.78 and 1.00. Since ω_p shifts only by 5% (Supplementary Fig. 9), m_b is essentially identical for these four substitutions. The frequency dependence of $m^{\star}(\omega)$ is rather weak in the range 2000–4000 cm^{-1}, i.e. around the Mott-Hubbard transitions. Towards low frequencies, however, $m^{\star}(\omega)$ exhibits a pronounced increase that eventually saturates at the static limit. This plateau corresponds to the effective mass of long-lived quasiparticles. Overall, our results reveal a frequency dependence of $m^{\star}/m_b$ similar to the optical data of the paradigmatic Fermi liquid Sr$_2$RuO$_4$ (cf. Supplementary Ref. 29, Fig. SM5) and iron pnictides (cf. Supplementary Ref. 30, Fig. 3b); we regard the agreement as a strong confirmation of this concept [25–27, 30–32]. As demonstrated in Fig. 3h, in the low-energy limit ($\omega \to 0$ and $T \to 0$) the effective mass enhancement follows the prefactor to the quadratic frequency dependence of the scattering rate, $\gamma \propto B\omega^2$, while approaching the Mott transition ($x = 1.00 \to 0.28$), yielding $B \propto (m^{\star}/m_b)^2$ in full accord with the Kadowaki-Woods relation [33].
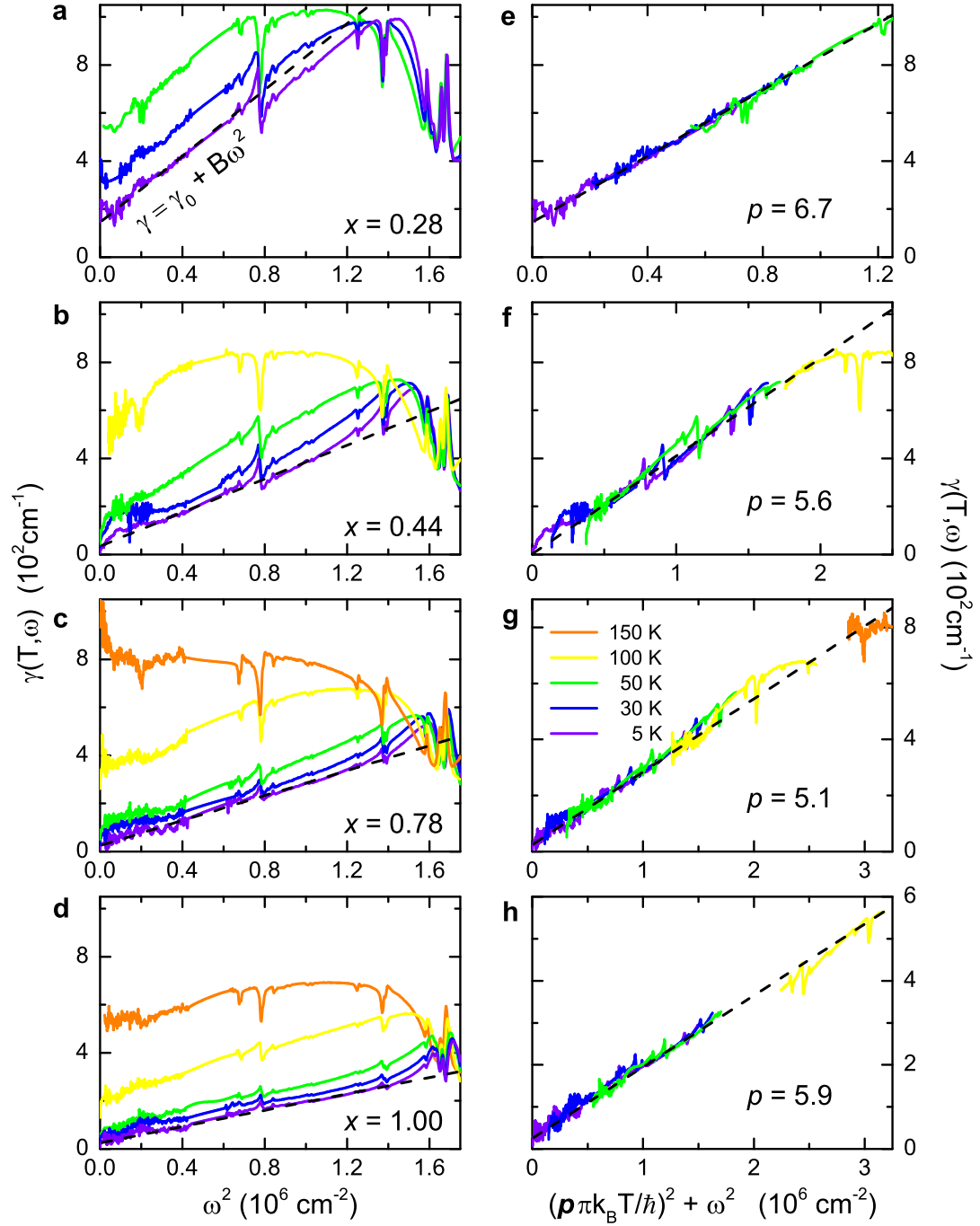
Supplementary Figure 9. **Dielectric loss function of κ-STF$_x$.** The plasma frequency is determined from the peak in the dielectric loss function $-\text{Im}\left\{\hat{\epsilon}^{-1}\right\}$ measured at $T = 5$ K. For all compounds κ-[(BEDT-STF)$_x$(BEDT-TTF)$_{1-x}$]$_2$Cu$_2$(CN)$_3$ we obtain $\omega_p \approx 4000$ cm^{-1}. It slightly increases with substitution indicating a general reduction of the band mass m_b.

Supplementary Figure 10. **Frequency-dependent effective mass of κ-STF$_x$.** The effective mass $m^\star/m_b$ of κ-[(BEDT-STF)$_x$(BEDT-TTF)$_{1-x}$]$_2$Cu$_2$(CN)$_3$ is determined as a function of frequency by performing an extended Drude analysis. In all cases the low-temperature $m^\star(\omega)/m_b$ increases towards low frequencies where it forms a plateau that corresponds to the quasiparticle mass in the limit $\omega \to 0$.

In Supplementary Fig. 11a-d we display the optical scattering rate $\gamma(T, \omega)$ for the compounds ($x = 0.28$, 0.44, 0.78, 1.00) that exhibit Fermi-liquid properties in their optical properties. Panels e-h display Gurzhi scaling on the generalized quadratic energy scale $(p\pi k_B T/\hbar)^2 + \omega^2$ [25–27, 34]. As indicated, we obtained a respective Gurzhi parameter $p = 6 \pm 1$ from our extended-Drude analysis.

Supplementary Figure 11. ω^2/T^2 **scaling of optical scattering rate. a-d,** $\gamma(T,\omega)$ is displayed for the substitutions $x = 0.28$, 0.44, 0.78, 1.00 on common axes. **e-h,** Renormalized to a generalized energy scale $(p\pi k_B T/\hbar)^2 + \omega^2$. Data are shown in the frequency range where Gurzhi scaling applies.

[1] Geiser, U. et al. Superconductivity at 2.8 K and 1.5 kbar in κ-(BEDT-TTF)$_2$Cu$_2$(CN)$_3$: the first organic superconductor containing a polymeric copper cyanide anion. Inorg. Chem. **30**, 2586–2588 (1991). URL http://dx.doi.org/10.1021/ic00012a005.

[2] Saito, Y., Minamidate, T., Kawamoto, A., Matsunaga, N. & Nomura, K. Site-specific ^{13}C NMR study on the locally distorted triangular lattice of the organic conductor κ-(BEDT-TTF)$_2$Cu$_2$(CN)$_3$. Phys. Rev. B **98**, 205141 (2018). URL `https://link.aps.org/doi/10.1103/PhysRevB.98.205141`.

[3] Kandpal, H. C., Opahle, I., Zhang, Y.-Z., Jeschke, H. O. & Valentí, R. Revision of Model Parameters for κ-Type Charge Transfer Salts: An Ab Initio Study. Phys. Rev. Lett. **103**, 067004 (2009). URL `https://link.aps.org/doi/10.1103/PhysRevLett.103.067004`.

[4] Kanoda, K. & Kato, R. Mott Physics in Organic Conductors with Triangular Lattices. Annu. Rev. Condens. Matter Phys. **2**, 167–188 (2011). URL `https://doi.org/10.1146/annurev-conmatphys-062910-140521`.

[5] Pustogow, A. et al. Low-Temperature Dielectric Anomaly Arising From Electronic Phase Separation at the Mott Insulator-Metal Transition. npj Quantum Mater. (2021). URL `https://doi.org/10.1038/s41535-020-00307-0`. arXiv:1907.04437

[6] Kurosaki, Y., Shimizu, Y., Miyagawa, K., Kanoda, K. & Saito, G. Mott Transition from a Spin Liquid to a Fermi Liquid in the Spin-Frustrated Organic Conductor κ-(BEDT-TTF)$_2$Cu$_2$(CN)$_3$. Phys. Rev. Lett. **95**, 177001 (2005). URL `https://link.aps.org/doi/10.1103/PhysRevLett.95.177001`.

[7] Furukawa, T., Miyagawa, K., Taniguchi, H., Kato, R. & Kanoda, K. Quantum criticality of Mott transition in organic materials. Nat. Phys. **11**, 221–224 (2015). URL `http://dx.doi.org/10.1038/nphys3235http://10.0.4.14/nphys3235http://www.nature.com/nphys/journal/v11/n3/abs/nphys3235.html{\#}supplementary-information`.

[8] Furukawa, T., Kobashi, K., Kurosaki, Y., Miyagawa, K. & Kanoda, K. Quasi-continuous transition from a Fermi liquid to a spin liquid in κ-(ET)$_2$Cu$_2$(CN)$_3$. Nat. Commun. **9**, 307 (2018). URL `https://doi.org/10.1038/s41467-017-02679-7`.

[9] Pustogow, A. et al. Quantum spin liquids unveil the genuine Mott state. Nat. Mater. **17**, 773–777 (2018). URL `https://doi.org/10.1038/s41563-018-0140-3`.

[10] Pinterić, M. et al. Anisotropic charge dynamics in the quantum spin-liquid candidate κ-(BEDT-TTF)$_2$Cu$_2$(CN)$_3$. Phys. Rev. B **90**, 195139 (2014). URL `https://link.aps.org/doi/10.1103/PhysRevB.90.195139`.

[11] Faltermeier, D. et al. Bandwidth-controlled Mott transition in κ-(BEDT-TTF)$_2$Cu[N(CN)$_2$]Br$_x$Cl$_{1-x}$: Optical studies of localized charge excitations. Phys. Rev. B **76**, 165113 (2007). URL `https://link.aps.org/doi/10.1103/PhysRevB.76.165113`.

[12] Merino, J., Dumm, M., Drichko, N., Dressel, M. & McKenzie, R. H. Quasiparticles at the Verge of Localization near the Mott Metal-Insulator Transition in a Two-Dimensional Material. Phys. Rev. Lett. **100**, 086404 (2008). URL `https://link.aps.org/doi/10.1103/PhysRevLett.100.086404`.

[13] Dumm, M. et al. Bandwidth-controlled Mott transition in κ-(BEDT-TTF)$_2$Cu[N(CN)$_2$]Br$_x$Cl$_{1-x}$: Optical studies of correlated carriers. Phys. Rev. B **79**, 195106 (2009). URL `https://link.aps.org/doi/10.1103/PhysRevB.79.195106`.

[14] Ferber, J., Foyevtsova, K., Jeschke, H. O. & Valentí, R. Unveiling the microscopic nature of correlated organic conductors: The case of κ-(BEDT-TTF)$_2$Cu[N(CN)$_2$]Br$_x$Cl$_{1-x}$. Phys. Rev. B **89**, 205106 (2014). URL `https://link.aps.org/doi/10.1103/PhysRevB.89.205106`.

[15] Dressel, M. & Drichko, N. Optical properties of two-dimensional organic conductors: signatures of charge ordering and correlation effects. Chem. Rev. **104**, 5689–716 (2004). URL `http://apps.webofknowledge.com/full{\_}record.do?product=UA{\&}search{\_}mode=GeneralSearch{\&}qid=39{\&}SID=T2ogN2hRfrXWYJZq9vq{\&}page=1{\&}doc=1`.

[16] Kézsmárki, I. et al. Depressed charge gap in the triangular-lattice Mott insulator κ-(ET)$_2$Cu$_2$(CN)$_3$. Phys. Rev. B **74**, 201101 (2006). URL `https://link.aps.org/doi/10.1103/PhysRevB.74.201101`.

[17] Elsässer, S., Wu, D., Dressel, M. & Schlueter, J. A. Power-law dependence of the optical conductivity observed in the quantum spin-liquid compound κ-(BEDT-TTF)$_2$Cu$_2$(CN)$_3$. Phys. Rev. B **86**, 155150 (2012). URL `https://link.aps.org/doi/10.1103/PhysRevB.86.155150`.

[18] Kanoda, K. Recent progress in NMR studies on organic conductors. Hyperfine Int. **104**, 235–249 (1997). URL `https://doi.org/10.1023/A:1012696314318`.

[19] McKenzie, R. H. A strongly correlated electron model for the layered organic superconductors κ-(BEDT-TTF)$_2 X$. Comments Cond. Matt. Phys. **18**, 309 (1998).

[20] Delacrétaz, L., Goutéraux, B., Hartnoll, S. & Karlsson, A. Bad Metals from Fluctuating Density Waves. SciPost Physics **3**, 25 (2017). URL `https://scipost.org/SciPostPhys.3.3.025`.

[21] Deng, X. et al. How Bad Metals Turn Good: Spectroscopic Signatures of Resilient Quasiparticles. Phys. Rev. Lett. **110**, 086401 (2013). URL `https://link.aps.org/doi/10.1103/PhysRevLett.110.086401`.

[22] Deng, X., Sternbach, A., Haule, K., Basov, D. N. & Kotliar, G. Shining Light on Transition-Metal Oxides: Unveiling the Hidden Fermi Liquid. Phys. Rev. Lett. **113**, 246404 (2014). URL `https://link.aps.org/doi/10.1103/PhysRevLett.113.246404`.

[23] Allen, J. W. & Mikkelsen, J. C. Optical properties of CrSb, MnSb, NiSb, and NiAs. Phys.Rev. B **15**, 2952–2960 (1977). URL `https://link.aps.org/doi/10.1103/PhysRevB.15.2952`.

[24] Dressel, M. & Grüner, G. Electrodynamics of Solids: Optical Properties of Electrons in Matter (Cambridge University Press, Cambridge, 2002). URL `http://www.netlibrary.com/urlapi.asp?action=summary{\&}v=1{\&}bookid=73043`.

[25] Maslov, D. L. & Chubukov, A. V. First-Matsubara-frequency rule in a Fermi liquid. II. Optical conductivity and comparison to experiment. Phys. Rev. B **86**, 155137 (2012). URL `https://link.aps.org/doi/10.1103/PhysRevB.86.155137`.

[26] Berthod, C. et al. Non-Drude universal scaling laws for the optical response of local Fermi liquids. Phys. Rev. B **87**, 115109 (2013). URL `https://link.aps.org/doi/10.1103/PhysRevB.87.115109`.

[27] Maslov, D. L. & Chubukov, A. V. Optical response of correlated electron systems. Rep. Prog. Phys. **80**, 026503 (2017). URL `http://stacks.iop.org/0034-4885/80/i=2/a=026503?key=crossref.e162a422a646a2aec909b8493a4387ba`.

[28] van Heumen, E. et al. Optical and thermodynamic properties of the high-temperature superconductor HgBa$_2$CuO$_{4+\delta}$. Phys.Rev. B **75**, 054522 (2007). URL `https://link.aps.org/doi/10.1103/PhysRevB.75.054522`.

[29] Stricker, D. et al. Optical Response of Sr$_2$RuO$_4$ Reveals Universal Fermi-Liquid Scaling and Quasiparticles Beyond Landau Theory. Phys. Rev. Lett. **113**, 087404 (2014). URL `https://link.aps.org/doi/10.1103/PhysRevLett.113.087404`.

[30] Tytarenko, A., Huang, Y., de Visser, A., Johnston, S. & van Heumen, E. Direct observation of a Fermi liquid-like normal state in an iron-pnictide superconductor. Sci. Rep. **5**, 012421 (2015). URL `https://doi.org/10.1038/srep12421http://10.0.4.14/srep12421https://www.nature.com/articles/srep12421{\#}supplementary-information`.

[31] Nagel, U. et al. Optical spectroscopy shows that the normal state of URu$_2$Si$_2$ is an anomalous Fermi liquid. Proc. Natl. Acad. Sci. **109**, 19161–19165 (2012). URL `http://www.pnas.org/content/109/47/19161.abstract`.

[32] Mirzaei, S. I. et al. Spectroscopic evidence for Fermi liquid-like energy and temperature dependence of the relaxation rate in the pseudogap phase of the cuprates. Proc. Natl. Acad. Sci. **110**, 5774 (2013). URL `http://www.pnas.org/content/110/15/5774.abstract`.

[33] Jacko, A. C., Fjaerestad, J. O. & Powell, B. J. A unified explanation of the Kadowaki-Woods ratio in strongly correlated metals. Nat. Phys. **5**, 422–425 (2009). URL `http://dx.doi.org/10.1038/nphys1249http://www.nature.com/nphys/journal/v5/n6/suppinfo/nphys1249{\_}S1.html`.

[34] Gurzhi, R. Mutual Electron Correlations in Metal Optics. J. Exp. Theor. Phys. **8**, 673 (1959). URL `http://www.jetp.ac.ru/cgi-bin/e/index/e/8/4/p673?a=list`.